Structure and iron-transporting mechanism of brain organic cation transporter 1

Jianan Chen[1,2,7], Shuhao Zhang[1,2,7], Wan Wei[3,7], Long Teng[1], Lei Tao[1,4], Kaixuan Gao[2,3], Bingqin Li[1], Aled M Edwards[5], Hao Fan[4,6]*, Xiangyu Liu[2,3]*, Ligong Chen[1,2,4]*

[1]State Key Laboratory of Membrane Biology, School of Pharmaceutical Sciences, Key Laboratory of Bioorganic Phosphorus Chemistry and Chemical Biology (Ministry of Education), Tsinghua University, Beijing, China.

[2]Beijing Frontier Research Center for Biological Structure, Tsinghua University, Beijing, China.

[3]Bioinformatics Institute (BII), Agency for Science, Technology and Research (A*STAR), Singapore, Republic of Singapore.

[4]Collaborative Innovation Center for Biotherapy, State Key Laboratory of Biotherapy and Cancer Center, West China Hospital, West China Medical School, Sichuan University, Chengdu, China.

[5]Structural Genomics Consortium, University of Toronto, Toronto, Canada.

[6]Synthetic Biology Translational Research Program, Yong Loo Lin School of Medicine, National University of Singapore, 10 Medical Drive, Singapore, and Duke-NUS Medical School, 8 College Rd, Singapore, Republic of Singapore.

[7]These authors contributed equally.

*Correspondence: fanh@bii.a-star.edu.sg; liu_xy@mail.tsinghua.edu.cn;

ligongchen@tsinghua.edu.cn

Abstract

Brain organic cation transporter 1 (BOCT1), also known as the solute carrier family 22 member 17 (SLC22A17) or the receptor for lipocalin-2 (LCN2), plays critical roles in health and disease. Its deficiency in mice results in early postnatal mortality and severe neurogenesis impairments. Despite its importance in physiology and pathophysiology, BOCT1's structure and transport mechanism remain elusive. Here, we integrate cryo-electron microscopy (cryo-EM), functional assays, biochemical experiments, and molecular dynamics simulations to elucidate the structure, substrate recognition, and transport mechanism of mouse BOCT1 (mBOCT1). The high-resolution cryo-EM structure reveals a distinctive N-terminal domain with a unique folding pattern dominated by a transmembrane loop atop TM6 (TML6), diverging from both known structures of SLC22 transporters and AlphaFold predictions. Notably, mBOCT1 functions as a high-capacity, low-affinity iron transporter independent of LCN2 binding. Iron transport is facilitated by a substrate gating mechanism involving TML6. These findings establish a structural basis for BOCT1's role as an independent iron transporter, enhancing our understanding of the transport mechanisms within major facilitator superfamily (MFS) transporters and providing new insights into brain iron homeostasis.

Introduction

45 As the second largest family of membrane proteins after G protein-coupled receptors
46 (GPCRs), solute carrier proteins (SLCs) are pivotal in numerous physiological
47 processes, including nutrient transport, neural signaling, immune responses, and tissue
48 homeostasis[1-3]. Brain organic cation transporter 1 (BOCT1), classified as SLC22A17
49 within the SLC22 family, is highly expressed in the brain[4,5]. Previous studies link
50 BOCT1 to cell apoptosis, multiple cancers, and Alzheimer's disease (AD)[6-9]. Recent
51 findings reveal that conditional knockout of mouse BOCT1 (mBOCT1) causes severe
52 weight loss, neural stem cell dysregulation, and early postnatal mortality,
53 underscoring its essential role in brain physiology (unpublished data).

54 BOCT1 is primarily recognized as the receptor for lipocalin-2 (LCN2), an
55 inflammatory mediator implicated in various pathologies[4]. LCN2 facilitates iron
56 transport by binding siderophores[4,10,11]. Devireddy et al. proposed that BOCT1 binds
57 iron-loaded LCN2, enhancing cellular iron levels via endocytosis, while binding to
58 iron-deficient LCN2 reduces intracellular iron through exocytosis, potentially
59 triggering cell apoptosis[4]. BOCT1 also interacts with other proteins, including
60 metallothionein (MT), transferrin, and albumin[7].

61 Compared to its role as a receptor, the transport mechanism and physiological
62 functions of BOCT1 remain largely unexplored. As an "orphan" transporter, BOCT1
63 does not transport the typical organic metabolites of the SLC22 family, and the
64 N-terminus of BOCT1 differs from other SLC22 members, as it lacks the typical
65 transmembrane helices 1 (TM1). Additionally, the over 100 amino acids preceding
66 the classical TM2 significantly differ from other proteins within the family

67 (Supplementary Fig. 1)[12]. Although the N-terminus has been suggested to be crucial
68 for the transport function of SLC22 family, discrepancies exist. For instance,
69 OCT1/SLC22A1 retains full transport activity despite losing its first two TMs[13,14].
70 Furthermore, structural predictions suggest BOCT1 may contain 9, 11, or 12 TMs,
71 reflecting uncertainty about its architecture[12,15].

72 To address these gaps, we determined the first 3D structure of mBOCT1 using
73 single-particle cryo-EM and validated its role as a distinct iron transporter through
74 protein liposome transport and cellular uptake assays. Integrating cryo-EM structure
75 with molecular dynamics (MD) simulations and site-directed mutagenesis, we
76 uncovered mBOCT1's substrate recognition and transport mechanism. This structural
77 and mechanistic characterization provides a framework for understanding intracellular
78 iron homeostasis and opens avenues for therapeutic targeting of BOCT1 in
79 neurological diseases associated with iron dysregulation.

80

81 **Results**

82 **Overall structure of mBOCT1**

83 The full-length mBOCT1, consisting of 520 amino acids and sharing 96.5% sequence
84 identity with human BOCT1 (Supplementary Fig. 2), was overexpressed in HEK293F
85 cells and purified for structural analysis. The mBOCT1 cryo-EM structure was
86 resolved to 3.3 Å overall resolution by single-particle analysis (Fig. 1a; Extended
87 Data Figs. 1a, b). The structure, solved with C2 symmetry, revealed an antiparallel
88 dimer configuration comprising 22 TMs (Extended Data Fig. 1). Further cell surface

89 staining assays with N- and C-terminal GFP-tagged mBOCT1 indicated that this
90 dimerization likely arises as an artifact of purification, with mBOCT1 adopting a
91 cohabiting form in detergent micelles to maintain a lower energy state. Consistent
92 with previous reports[12], the N-terminus faces the extracellular side, while the
93 C-terminus faces the intracellular side (Extended Data Fig. 2a). Interestingly, over 90
94 N-terminal residues remain unresolved in the cryo-EM structure, aligning with NMR
95 studies that classify the N-terminus as an intrinsically disordered region (IDR)[12].

96 Transporters in the MFS typically possess 12 TMs with two-fold
97 pseudosymmetry between their N-terminal domain (NTD; TM1-TM6) and C-terminal
98 domain (CTD; TM7-TM12) [16]. However, mBOCT1 comprises only 11 TMs,
99 corresponding to TM2-TM12 of canonical MFS transporters. TM2-TM6 form the
100 NTD, while TM7-TM12 constitute the CTD (Figs. 1a, b). Notably, the NTD and CTD
101 of mBOCT1 lack the characteristic pseudosymmetry of MFS transporters due to
102 distinct orientations of TM5-TM6 and TM11-TM12, which are usually aligned among
103 other MFS members (Fig. 1c). Structural prediction corroborates the existence of a
104 minority subset of MFS members with 11 TMs[16], as evidenced by the crystal structure
105 of human equilibrative nucleoside transporter 1 (hENT1) [17] that lacks TM12, while
106 mBOCT1 lacks TM1.

107 A distinguishing feature of mBOCT1 is a disordered transmembrane loop
108 (TML6; residues 220–236) located above TM6 in the cryo-EM structure, unlike
109 homologous regions in experimental structures of other SLC22 members or
110 AlphaFold3 predictions, which depict this segment as an intact helix distant from the

transport pathway (Figs. 1b, c; Extended Data Fig. 2b). Nevertheless, sequence-based structural predictions suggest that TML6 might adopt a helical conformation under specific conditions (Supplementary Text in SI; Supplementary Fig. 3), and MD simulations reveal that TML6 can remain stable in both loop and helix forms (Extended Data Fig. 3a; Supplementary Table 4). Therefore, we speculate that mBOCT1's TML6 may undergo conformational transitions between unique functional states (Extended Data Fig. 3a). The structural stability and helicity of all TMs of mBOCT1 in all-atom MD simulations show that TML6 is less stable than other TMs, and is more likely to undergo conformational rearrangements (Extended Data Fig. 3b). Moreover, TM6 had its helix elongated into the cytoplasm during certain segments of MD simulations (Extended Data Fig. 3c). Collectively, we speculate that substrate transport of mBOCT1 is accompanied by conformational changes of both TML6 and TM6.

Substrate Identification of mBOCT1

Electrostatic analysis reveals that the transport cavity of mBOCT1 is negatively charged, similar to the organic cation transporter OCT1[18] and the Fe^{2+} efflux transporter hFPN1[19], but distinct from the organic anion transporter OAT1 (Fig. 2a; Extended Data Figs. 4a, b)[20]. This suggests that mBOCT1 likely transports positively charged substrates. The binding pocket of mBOCT1 also exhibits hydrophilic characteristics similar to that of hFPN1[19], but differs from those of OCT1 and OAT1 (Extended Data Figs. 4a, c)[18,20]. Conservation analysis performed using Consurf

133 highlights significant differences in mBOCT1's binding pocket compared to other
134 SLC22 family members (Fig. 2b).

135 We observe an additional density within the binding pocket, and the binding
136 pocket comprises a mix of polar and aromatic residues suitable for metal ion
137 coordination, including Y115, D169, and E193 in close proximity and H319 slightly
138 farther away (Figs. 2a, c). Using inductively coupled plasma mass spectrometry
139 (ICP-MS), we identified iron as the predominant metal ion associated with mBOCT1
140 protein samples analyzed via cryo-EM (Fig. 2d).

141 To validate its metal ion transport activity, we conducted a cellular uptake assay
142 using calcein quenching. mBOCT1-expressing HEK293T cells exhibited 2–3 times
143 greater $FeCl_2$ transport activity compared to empty vector (EV) controls, with similar
144 results for $FeSO_4$ (Fig. 2e; Extended Data Fig. 5). Protein-liposome transport assays
145 further confirmed mBOCT1's ability to transport $FeCl_2$ with a Michaelis-Menten
146 constant (K_m) of 2.7 ± 1.0 mM and V_{max} of -1.44 x10^{-2} ΔF s^{-1} (Fig. 2f). mBOCT1
147 liposomes also transported other metal ions, including Mn^{2+} and Co^{2+} (Extended Data
148 Figs. 6a-c). In addition, Microscale thermophoresis (MST) assays that measure
149 binding affinities, revealed a dissociation constant (k_d) of 0.43 μM for $FeCl_2$,
150 comparable to $CuCl_2$ and $MnCl_2$, while $CoCl_2$ exhibited a higher binding affinity (Fig.
151 2g; Extended Data Fig. 6d). These findings establish mBOCT1 as a transporter for
152 multiple divalent metal ions, facilitating their cellular uptake independently.

153

154 **Molecular basis of mBOCT1 substrate recognition**

155 To confirm the iron-binding site identified in the mBOCT1 cryo-EM structure, we
156 introduced mutations in the putative binding pocket and measured their $FeCl_2$
157 transport activity. Mutations D169A, D169T, and E193A resulted in substantially
158 reduced activity (~20% of wildtype [WT]), highlighting the critical role of the
159 negative charges on D169 and E193 in facilitating iron transport. Y115 likely
160 interacts with iron through polar and cation-π interactions, as the Y115F mutant
161 retained ~40% of WT activity (Fig. 3a). MD simulations supported this, showing that
162 Fe^{2+} remained stable at this site (Figs. 3b, c; Supplementary Table 5) and frequently
163 interacted with the binding site residues (Supplementary Table 6).
164 Mutating polar residues along the transport pathway (e.g., Y173A, H200A, H323A,
165 T413V, Supplementary Fig. 4) significantly impaired $FeCl_2$ transport, underscoring
166 their pivotal roles. H319A displayed impaired activity similar to D169A and E193A,
167 while H319F retained ~60% of WT activity, suggesting that H319 contributes through
168 polar and cation-π interactions. However, the H319W mutation caused significant
169 activity loss, likely due to steric hindrance. Similarly, H200F and H323F mutations
170 had less severe reductions in activity than their alanine counterparts, possibly due to
171 favorable cation-π interactions with aromatic rings (Fig. 3d). These key residues are
172 conserved in human and mouse BOCT1 but not in other SLC22 family members,
173 indicating functional conservation across species (Fig. 3e).
174
175 **Iron transport gating mechanism of mBOCT1**
176 In the mBOCT1 cryo-EM structure, the negatively charged residue D336 is

177 positioned at the entrance of the proposed transport pathway, formed by the NTD and
178 CTD (Fig. 2a). The D336A mutation reduced $FeCl_2$ transport activity to ~40% of WT
179 levels (Fig. 3d), suggesting that D336 acts as a "hook" to attract iron, a hypothesis
180 supported by MD simulations (Extended Data Fig. 7a, Supplementary Movie 1).

181 mBOCT1's TML6 is situated at the entrance of the transport pathway, differing
182 from the mBOCT1 AlphaFold3 model or experimental structures of other SLC22
183 family members (Fig. 1)[21]. mBOCT1 features a unique GGGG (329-332) motif,
184 which is rare within the SLC22 family (Extended Data Fig. 2b). These four
185 consecutive glycine residues are situated near TML6 along the transport pathway. The
186 TML6 and GGGG motif constitute an extracellular gate for mBOCT1 (Figs. 4a, b). In
187 MD simulations based on the cryo-EM structure, Fe^{2+} was unable to penetrate the
188 pathway unless TML6 moved away to allow substrate entry, emphasizing TML6's
189 role in gating (Figs. 4a, c; Supplementary Fig. 5). TML6 is stabilized by hydrophobic
190 interactions between F229 (TML6) and F107/F111 (TM2), that possibly contributes
191 to the transporter's occluded conformation (Figs. 4a, d). On the intracellular side,
192 Y173 and T413 form sidechain hydrogen bonds and may act as a gate, controlling
193 Fe^{2+} release into the cell (Figs. 4a, e).

194

195 **Protonation on iron transport in mBOCT1**

196 Mutating E193 to aspartate or asparagine did not affect transport activity, while
197 replacing it with arginine enhanced activity (Fig. 4f). This indicates that the
198 protonation state of E193 affects Fe^{2+} release, as supported by parallel cascade

199 selection molecular dynamics (PaCS-MD) simulations (Supplementary Table 2). In
200 these simulations, protonation of D169 or E193 increased the distance between these
201 two residues, allowing greater Fe^{2+} mobility within the transport pathway (Fig. 4g), as
202 indicated by the altered angle formed by Fe^{2+}, D169, and E193 (Extended Data Fig.
203 7b). The average and maximum Fe^{2+} ion depth in the lipid bilayer also increased
204 (Supplementary Table 7). Thus, the Fe^{2+} ion is more likely to be released from the
205 binding pocket when D169 or E193 is protonated.

206 In addition, MD simulations revealed that Fe^{2+} is consistently surrounded by a
207 hydration shell of 5-6 water molecules (Extended Data Figs. 7c, d), which forms
208 hydrogen bonds with D169 and E193. Protonation of these two residues would disrupt
209 these hydrogen bonds and facilitate Fe^{2+} release, with a more pronounced effect upon
210 E193 protonation, which affected water hydrogen bonding with both D169 and E193.
211 In contrast, D169 protonation disrupted only its own hydrogen bonds with water
212 (Extended Data Figs. 7d, e). A recent study has demonstrated that the protonation and
213 deprotonation of D/E residues regulate extracellular gating in a homologous organic
214 anion transporter, SLC17[22], supporting our hypothesis that D/E residue protonation
215 influences mBOCT1 iron transport. However, further studies are needed to fully
216 elucidate this mechanism.

217

218 **Fe^{2+} transport model of mBOCT1**

219 Structural comparisons between the "outward-open" hOCT1[21], "inward-open"
220 hOCT1[23], and mBOCT1 reveal that TML6 in mBOCT1 aligns spatially with TM1,

221 rather than TM6 of classic MFS transporters (Extended Data Figs. 8a, b). Given the
222 established importance of conformational changes in TM1 for substrate transport in
223 classic MFS transporters[16], this highlights the critical role of TML6 in mBOCT1
224 substrate transport. Additionally, conformational changes in TM7 and TM10 of
225 mBOCT1 are likely integral to the transport process (Extended Data Figs. 8a, b). The
226 aforementioned changes were also observed when we conducted structural alignments
227 between the homology modeling-generated outward-open mBOCT1 model,
228 inward-open mBOCT1 model, and the cryo-EM structure of the occluded mBOCT1
229 (Supplementary Fig. 6; Supplementary Text in SI).

230 Building on these observations and the rocker-switch substrate transport
231 mechanism of MFS transporters, we propose a new Fe^{2+} transport model for
232 mBOCT1. Initially, in the hypothesized outward-open conformation, TML6 and the
233 GGGG motif orient away from the transport pathway, leaving the extracellular gate
234 open. Fe^{2+}, attracted by electrostatic interactions with negatively charged residues
235 such as D336, enters the pathway. Subsequently, interactions between TML6 and
236 other TMs shift TML6 toward the transport pathway, preventing further substrate
237 entry. The extracellular gate is sealed by a hydrogen bond between I225 on TML6
238 and R322 on TM7.

239 Once inside, Fe^{2+} is progressively guided downward by polar residues such as
240 H200 and H319, followed by negatively charged residues D169 and E193.
241 Protonation of D169 or E193 likely triggers conformational changes in TM7 and
242 TM10 of the CTD, potentially coupled with TM6 extending into the cytoplasm. This

243 facilitates the opening of the intracellular gate, formed by hydrogen bonds involving
244 Y173 and T413, allowing Fe^{2+} release into the cell and completing the transport cycle
245 (Fig. 5).
246

247 **Discussion**

248 This study presents the high-resolution cryo-EM structure of mBOCT1 in complex
249 with endogenous Fe^{2+} in its occluded conformation. Unlike typical MFS transporters,
250 which exhibit pronounced pseudosymmetry between their NTD and CTD[16],
251 mBOCT1's NTD and CTD adopt folding patterns that diverge significantly from
252 other MFS members.

253 Notably, mBOCT1 demonstrates the ability to transport Fe^{2+} independently of
254 LCN2. Previous studies suggest that LCN2 binds to siderophores and facilitates Fe^{3+}
255 transport via BOCT1[4]. However, our findings indicate that mBOCT1 selectively
256 transports divalent metal ions such as Fe^{2+}, highlighting its dual functionality:
257 receptor-mediated Fe^{3+} transport and transporter-mediated Fe^{2+} transport. The
258 substrate affinity (K_m) for Fe^{2+}, determined via liposome transport assays, is
259 approximately 2.7 mM—considerably lower than the K_m of 13.6 μM reported for the
260 classical Fe^{2+} efflux transporter hFPN1 (SLC40A1)[19]. Conversely, mBOCT1's Fe^{2+}
261 binding dissociation constant (k_d), measured by MST, is ~0.43 μM, significantly
262 stronger than the 30 μM k_d observed in the bivalent metal transporter ScaDMT
263 (SLC11 family)[24]. These results classify mBOCT1 as a "High Capacity, Low
264 Affinity" transporter, akin to the OCT family, in contrast to the "High Affinity, Low

265 Capacity" transporters of the SLC6 family[25,26].

266 Unlike other SLC22 family members, which primarily recognize substrates
267 through aromatic residues such as Y230 and F438 in OAT1 or Y36/Y37 and
268 Y361/Y362 in OCT1-2[20,21], mBOCT1 engages residues Y115, D169, and E193 for
269 Fe^{2+} recognition. Additionally, while TM7, TM10, TM11, and intracellular loop (ICH)
270 regions in OCTs and the aromatic residues Y353 and F442 in OAT1 facilitate
271 substrate transport through conformational changes[20,23], our data suggest that
272 mBOCT1 employs a unique mechanism where TML6 serves as a pivotal gating
273 element (Fig. 4, 5).

274 Sequence alignment further supports that hBOCT1 likely mirrors mBOCT1's
275 transport mechanism, given the high conservation of key residues involved in
276 substrate recognition (Y115, D169, E193), TML6 folding (F107, F111, F229), and the
277 formation of the GGGG motif. In contrast, corresponding homologous residues in
278 human and mouse OCT1, OCT3, and OAT1 show limited conservation, with the
279 exception of F111 (Fig. 3e; Extended Data Fig. 2b). This divergence underpins the
280 functional differences between BOCT1 and other SLC22 family members.

281 In summary, this study identifies Fe^{2+} as the direct substrate of BOCT1,
282 delineates key residues involved in substrate recognition and transport, and proposes a
283 distinct molecular transport mechanism. Our findings advance the "de-orphaning" of
284 the SLC transporter family and highlight BOCT1 as a potential therapeutic target for
285 iron metabolism and homeostasis-related disorders. Dysregulation of iron homeostasis
286 is closely linked to neurodegenerative diseases such as multiple sclerosis, Parkinson’s

287 disease, and Alzheimer's disease[27-29]. The structural and functional insights provided
288 here deepen our understanding of these pathologies and may guide rational drug
289 design. Finally, while AlphaFold[30,31] has achieved remarkable accuracy in structure
290 prediction, the unexpected cryo-EM structure of BOCT1 underscores the
291 indispensable role of traditional structural biology methods.
292

293 **References**

294 1 Chen, R. & Chen, L. Solute carrier transporters: emerging central players in
295 tumour immunotherapy. *Trends Cell Biol* **32**, 186-201 (2022).
296 2 Chi, W. *et al.* MCT1-governed pyruvate metabolism is essential for antibody
297 class-switch recombination through H3K27 acetylation. *Nat Commun* **15**, 163 (2024).
298 3 Wang, W. W., Gallo, L., Jadhav, A., Hawkins, R. & Parker, C. G. The
299 Druggability of Solute Carriers. *J Med Chem* **63**, 3834-3867 (2020).
300 4 Devireddy, L. R., Gazin, C., Zhu, X. & Green, M. R. A cell-surface receptor for
301 lipocalin 24p3 selectively mediates apoptosis and iron uptake. *Cell* **123**, 1293-1305
302 (2005).
303 5 Bennett, K. M., Liu, J., Hoelting, C. & Stoll, J. Expression and analysis of two
304 novel rat organic cation transporter homologs, SLC22A17 and SLC22A23. *Mol Cell*
305 *Biochem* **352**, 143-154 (2011).
306 6 Chi, Y. *et al.* Cancer cells deploy lipocalin-2 to collect limiting iron in
307 leptomeningeal metastasis. *Science* **369**, 276-282 (2020).

308 7 Langelueddecke, C. *et al.* Lipocalin-2 (24p3/neutrophil gelatinase-associated
309 lipocalin (NGAL)) receptor is expressed in distal nephron and mediates protein
310 endocytosis. *J Biol Chem* **287**, 159-169 (2012).
311 8 Lee, M. *et al.* Genome-wide association study for the interaction between BMR
312 and BMI in obese Korean women including overweight. *Nutr Res Pract* **10**, 115-124
313 (2016).
314 9 Dekens, D. W. *et al.* Neutrophil Gelatinase-Associated Lipocalin and its
315 Receptors in Alzheimer's Disease (AD) Brain Regions: Differential Findings in AD
316 with and without Depression. *J Alzheimers Dis* **55**, 763-776 (2017).
317 10 Goetz, D. H. *et al.* The neutrophil lipocalin NGAL is a bacteriostatic agent that
318 interferes with siderophore-mediated iron acquisition. *Mol Cell* **10**, 1033-1043 (2002).
319 11 Yang, J. *et al.* An iron delivery pathway mediated by a lipocalin. *Mol Cell* **10**,
320 1045-1056 (2002).
321 12 Cabedo Martinez, A. I. *et al.* Biochemical and Structural Characterization of the
322 Interaction between the Siderocalin NGAL/LCN2 (Neutrophil Gelatinase-associated
323 Lipocalin/Lipocalin 2) and the N-terminal Domain of Its Endocytic Receptor
324 SLC22A17. *J Biol Chem* **291**, 2917-2930 (2016).
325 13 Burckhardt, G. & Wolff, N. A. Structure of renal organic anion and cation
326 transporters. *Am J Physiol Renal Physiol* **278**, F853-866 (2000).
327 14 Zhang, L., Dresser, M. J., Chun, J. K., Babbitt, P. C. & Giacomini, K. M. Cloning
328 and functional characterization of a rat renal organic cation transporter isoform
329 (rOCT1A). *J Biol Chem* **272**, 16548-16554 (1997).

330 15 Jacobsson, J. A., Haitina, T., Lindblom, J. & Fredriksson, R. Identification of six
331 putative human transporters with structural similarity to the drug transporter SLC22
332 family. *Genomics* **90**, 595-609 (2007).
333 16 Drew, D., North, R. A., Nagarathinam, K. & Tanabe, M. Structures and General
334 Transport Mechanisms by the Major Facilitator Superfamily (MFS). *Chem Rev* **121**,
335 5289-5335 (2021).
336 17 Wright, N. J. & Lee, S. Y. Structures of human ENT1 in complex with adenosine
337 reuptake inhibitors. *Nat Struct Mol Biol* **26**, 599-606 (2019).
338 18 Zhang, S. *et al.* Structural insights into human organic cation transporter 1
339 transport and inhibition. *Cell Discov* **10**, 30 (2024).
340 19 Billesbølle, C. B. *et al.* Structure of hepcidin-bound ferroportin reveals iron
341 homeostatic mechanisms. *Nature* **586**, 807-811 (2020).
342 20 Dou, T., Lian, T., Shu, S., He, Y. & Jiang, J. The substrate and inhibitor binding
343 mechanism of polyspecific transporter OAT1 revealed by high-resolution cryo-EM.
344 *Nat Struct Mol Biol* **30**, 1794-1805 (2023).
345 21 Suo, Y. *et al.* Molecular basis of polyspecific drug and xenobiotic recognition by
346 OCT1 and OCT2. *Nat Struct Mol Biol* **30**, 1001-1011 (2023).
347 22 Dmitrieva, N. *et al.* Transport mechanism of DgoT, a bacterial homolog of
348 SLC17 organic anion transporters. Preprint at bioRxiv (2024).
349 23 Zeng, Y. C. *et al.* Structural basis of promiscuous substrate transport by Organic
350 Cation Transporter 1. *Nat Commun* **14**, 6374 (2023).

351 24 Ehrnstorfer, I. A., Geertsma, E. R., Pardon, E., Steyaert, J. & Dutzler, R. Crystal
352 structure of a SLC11 (NRAMP) transporter reveals the basis for transition-metal ion
353 transport. *Nat Struct Mol Biol* **21**, 990-996 (2014).
354 25 Koepsell, H. Organic Cation Transporters in Health and Disease. *Pharmacol Rev*
355 **72**, 253-319 (2020).
356 26 Kristensen, A. S. *et al.* SLC6 neurotransmitter transporters: structure, function,
357 and regulation. *Pharmacol Rev* **63**, 585-640 (2011).
358 27 Singh, N. *et al.* Brain iron homeostasis: from molecular mechanisms to clinical
359 significance and therapeutic opportunities. *Antioxid Redox Signal* **20**, 1324-1363
360 (2014).
361 28 Ward, R. J., Zucca, F. A., Duyn, J. H., Crichton, R. R. & Zecca, L. The role of
362 iron in brain ageing and neurodegenerative disorders. *Lancet Neurol* **13**, 1045-1060
363 (2014).
364 29 Zucca, F. A. *et al.* Interactions of iron, dopamine and neuromelanin pathways in
365 brain aging and Parkinson's disease. *Prog Neurobiol* **155**, 96-119 (2017).
366 30 Jumper, J. *et al.* Highly accurate protein structure prediction with AlphaFold.
367 *Nature* **596**, 583-589 (2021).
368 31 Abramson, J. *et al.* Accurate structure prediction of biomolecular interactions
369 with AlphaFold 3. *Nature* **630**, 493-500 (2024).
370

371 **Methods**

372 **Protein expression and purification of mBOCT1**

373 The mBOCT1 protein (NCBI: NP_001347335.1), tagged at the C-terminus with
374 either a strep tag or GFP and a 3C protease cleavage site, was cloned into the
375 pcDNA3.1(+) vector. The recombinant plasmid, free from endotoxins, was
376 transfected into HEK293F cells using PEI at a 3:1 mass ratio. After 48 hours, cells
377 were harvested and lysed using a buffer containing 20 mM Tris-HCl pH 8.0, 2 mM
378 EDTA, and protease inhibitors. The lysate was centrifuged, and the resulting pellet
379 was solubilized in 20 mM Hepes pH 8.0, 100 mM NaCl, 1% (w/v) MNG, 0.1% (w/v)
380 CHS, and protease inhibitors before further centrifugation at 18,000 rpm.

381 The supernatant was applied to strep affinity beads and homemade anti-GFP
382 nanobody Sepharose beads, equilibrated and rinsed in 20 mM Hepes pH 8.0, 100 mM
383 NaCl, 0.01% (w/v) MNG, and 0.001% (w/v) CHS. For strep-tagged mBOCT1, the
384 protein was eluted with the same buffer supplemented with 2.5 mM Desthiobiotin.
385 For GFP-tagged mBOCT1, the tag was removed using 3C protease. The eluted
386 protein was concentrated with a 50-kDa MWCO Millipore concentrator and subjected
387 to size-exclusion chromatography (SEC) using a Superdex 200 Increase column (GE)
388 equilibrated in 20 mM Hepes pH 8.0, 100 mM NaCl, 1 mM TCEP, 0.003% (w/v)
389 MNG, and 0.0003% (w/v) CHS. Peak fractions were collected for experiments, and
390 purity was confirmed by SDS-PAGE.

391

392 **Cryo-EM sample preparation and data collection**

393 Purified mBOCT1 peak fractions were concentrated to 5 mg mL^{-1}. Four µL of the
394 sample was applied to glow-discharged Quantifoil gold 200 mesh grids (R1.2/1.3),
395 blotted for 4.5 s and waited for 5 s, and plunge-frozen in liquid ethane using a FEI
396 Mark IV Vitrobot at 8 °C and 100% humidity. Data collection was performed on a
397 300 kV Titan Krios G3i equipped with a BioQuantum K3 camera. Movies were
398 recorded at 50 $e^{-}/Å^{2}$ with a defocus range of -1.2 to -1.5 µm. A total of 4,649
399 micrographs were collected with a magnification of 64,000x, corresponding to a pixel
400 size of 1.08 Å.
401
402 **Cryo-EM data processing**
403 Data were processed using cryoSPARC 3.2 and 4.1[32]. An initial 185 micrographs
404 underwent patch CTF estimation, and micrographs with estimated CTF resolutions
405 worse than 4 Å were excluded after checked by manual curate exposure. After two
406 rounds of 2D classification, selected classes were used for template picking in the
407 entire set of 4649 micrographs, yielding 7,433,396 particles extracted at 256 pixels
408 and downsampled to 128 pixels. Ab initio models were generated from good classes
409 or bad classes, followed by heterogeneous refinement to remove suboptimal particles.
410 The final dataset consisted of 360,940 particles re-extracted at 256 pixels, then the 2D
411 classification and heterogenous refinement were repeated, and 171,512 particles were
412 used for final refinement. Local CTF refinement was applied to per-particle. Finally, a
413 3.3 Å C2 symmetry density map was obtained.
414

415 **Model building and refinement**

416 The initial mBOCT1 model was generated using cyronet.ai and AlphaFold, followed
417 by iterative refinement in Coot and real-space refinement in PHENIX[33,34]. Validation
418 was performed using PHENIX and MolProbity, with figures generated in PyMOL and
419 ChimeraX[35].

420

421 **Identification of metal element content in purified mBOCT1 protein**

422 The metal content of purified mBOCT1 was analyzed via ICP-MS (Agilent
423 Technologies). Equal volumes of 1.2 mg mL^{-1} mBOCT1 and control buffer were
424 mixed with 100 μL of high-purity nitric acid and heated for 4 hours in a water bath.
425 The reaction mixtures were adjusted to a final volume of 5 mL and analyzed via
426 ICP-MS.

427

428 **Surface staining by immunofluorescence**

429 HEK293T cells were stably transfected with mBOCT1 constructs tagged with GFP at
430 the N-terminus or C-terminus or an empty vector (EV). Cells were seeded on
431 poly-D-lysine-coated slides and blocked with 1% BSA at room temperature for 30
432 minutes. Cells were stained with 100 nM Alexa647-GFP nanobody, washed with PBS,
433 and fixed with 4% PFA. Nuclei were counterstained with 1 μg μL^{-1} DAPI, and slides
434 were sealed with an anti-fluorescent quencher agent. Samples were imaged using an
435 Olympus FV3000 confocal microscope.

436

437 **Construction of mBOCT1 stable cell line**

438 The wild-type (WT) and mutant mBOCT1 constructs, each bearing an N-terminal HA
439 and Flag tag, were cloned into the lentiviral vector pLJM1. The recombinant pLJM1
440 plasmid, along with the packaging plasmids pMD2.G and psPAX2 (mass ratio 5:3:2),
441 was co-transfected into HEK293T cells using PEI. Lentiviral supernatants from these
442 cells were harvested and used to infect fresh HEK293T and CHO cells. Puromycin
443 (Beyotime) was added at appropriate concentrations to select for positively
444 transfected cells. After a two-week screening process, surviving cells were deemed
445 successfully transfected. For GFP-tagged mBOCT1 constructs, an additional step of
446 positive cell sorting was performed using a FACSAriaII (BD). Overexpression
447 efficiency was confirmed via qPCR and western blot.

448

449 **Cellular substrate uptake assay**

450 Stable HEK293T and CHO cell lines expressing mBOCT1 with N-terminal HA and
451 Flag tags, as well as cells transfected with the empty vector (pLJM1), were seeded
452 into 96-well plates. On the day of the assay, cells were washed with PBS, followed by
453 the addition of 100 μL calcein-AM (1 μM, diluted in serum-free medium) and
454 incubation at 37 °C for 40 minutes. The dye solution was removed, and the cells were
455 incubated in fresh serum-free medium at 37 °C for another 40 minutes to ensure the
456 complete conversion of non-fluorescent calcein-AM to fluorescent calcein. After
457 washing with HBSS (without calcium and magnesium), baseline fluorescence was
458 recorded using a microplate reader (excitation: 490 nm, emission: 520 nm) for at least

459 1 minute. Subsequently, 10 μL of a solution containing metal ions diluted in HBSS
460 (without calcium and magnesium) was added, and the uptake curve was measured
461 over 4 minutes.

462 For dose-response experiments, $FeCl_2$ concentrations ranged from 1 μM to 500
463 μM. For iron transport assays with mBOCT1 mutants, Fe^{2+} and other metal ions were
464 used at final concentrations of 2 μM. Sodium ascorbate was added at a 20-fold molar
465 ratio to ferric ions to maintain a reductive environment. Each experiment was
466 independently repeated in triplicate, and data were analyzed using GraphPad Prism.

467

468 **Protein liposome assembly**

469 Protein liposome preparation followed the method by Billesbølle et al [19]. Lipids POPE
470 and POPG were dissolved in chloroform (mass ratio 3:1), dried under argon gas,
471 resuspended in an internal buffer (20 mM HEPES, pH 7.4, and 100 mM KCl), and
472 sonicated. The lipid mixture underwent repeated freeze-thaw cycles and extrusion
473 through a 400 nm polycarbonate filter. To destabilize liposomes, 0.13% (w/v)
474 Triton-X-100 was added, followed by purified mBOCT1 (lipid-to-protein ratio of
475 40:1). After incubation at 4 °C for 30 minutes, SM2-Biobeads (0.05 mg/mL) were
476 used to remove detergent over a 1-hour period. This process was repeated overnight,
477 followed by a final incubation with 0.08 mg/mL SM2-Biobeads for 2 hours at 4 °C.
478 Protein liposomes were collected by centrifugation at 246,000 × *g* for 30 minutes,
479 resuspended in internal buffer, and frozen by liquid nitrogen, and then stored at
480 -80 °C. A control sample, prepared without purified mBOCT1, was similarly

481 processed.

482

483 **Protein liposome-based transport assay**

484 On the experiment day, liposomes were thawed and resuspended at 2 mg/mL in an
485 internal buffer containing 250 μM calcein. Liposomes were subjected to repeated
486 freeze-thaw cycles, extrusion, and concentration at 264,000 × *g* for 30 minutes.
487 Calcein-containing liposomes were washed with an external buffer (20 mM HEPES,
488 pH 7.4, and 100 mM NaCl).

489 During the assay, 100 nM valinomycin was added to establish a membrane
490 potential. Liposomes were added to a final concentration of 0.1 mg/mL. For
491 dose-response experiments, $FeCl_2$ concentrations ranged from 0.05 μM to 5 mM.
492 Other metal ions were tested at 1 mM. Sodium ascorbate (20-fold molar ratio) was
493 included to maintain a reductive environment for ferric ions. Fluorescence was
494 recorded at 2–3 s intervals (excitation: 490 nm, emission: 520 nm) over at least 1
495 minute. Transport was terminated by adding 10 μM calcimycin, and data were
496 collected using a microplate reader. All experiments were independently repeated in
497 triplicate, and results were analyzed with GraphPad Prism.

498

499 **Binding assay of mBOCT1 with substrates**

500 The binding interaction between mBOCT1 and metal ions was analyzed using MST.
501 Purified mBOCT1 was labeled with a Monolith™ RED-NHS secondary generation
502 protein labeling kit, and unbound dye was removed following the manufacturer's

503 protocol. Prior to labeling, mBOCT1 underwent buffer exchange to minimize TCEP
504 interference, using a replacement buffer containing 20 mM Hepes pH 8.0, 100 mM
505 NaCl, 0.003% (w/v) MNG, and 0.0003% (w/v) CHS.

506 For the assay, 10 μM mBOCT1 was labeled, and 40 nM of the labeled protein
507 was mixed with serial dilutions of $CoCl_2$ (25 μM to 1.5 nM) and other metal ions (100
508 μM to 3.1 nM). To ensure a reductive environment for ferric ions, sodium ascorbate
509 was added at a 20-fold molar ratio. The mixtures were centrifuged at 13,000 rpm and
510 loaded into Monolith™ NT115 capillaries (K-022). The MST experiments were
511 conducted under medium power and 60% auto-detection using the Monolith™
512 NT115 system from NanoTemper Technologies. Data were analyzed with
513 Mo.Affinity Analysis software (X86), and each experiment was independently
514 repeated three times.

515

516 **Modeling of TML6 and unresolved intracellular domain by MD simulations**

517 The experimentally determined structure was refined using the Bayesian
518 inference-based EMMIVox approach implemented in PLUMED (www.plumed.org)
519 [36,37]. Missing atoms were reconstructed using the CHARMM-GUI web server[38,39],
520 which also generated topology files. The cryo-EM map was aligned with the
521 reconstructed conformation in PLUMED format.

522 Structural refinement involved minimization and equilibration (1 ns NPT,
523 followed by 2 ns NVT) at 300 K, with position restraints of 400 kJ/(mol·nm^2) on the
524 protein backbone and 40 kJ/(mol·nm^2) on sidechain heavy atoms. The NVT

525 equilibration trajectory was used to optimize the scaling factor between the
526 experimental cryo-EM map and the derived map. A 10 ns NVT production run
527 followed, applying restraints from the cryo-EM map. The conformation with the
528 lowest EMMIVox hybrid energy was extracted along with its B-factors. This
529 conformation underwent steepest descent energy minimization, sampling B-factors
530 via a modified Monte Carlo approach. The final minimized structure was re-aligned to
531 the original cryo-EM map, with sampled B-factors incorporated to generate a
532 complete PDB file containing heavy atoms only. This refined cryo-EM model was
533 used for following modeling and simulations. All simulations were performed using
534 GROMACS 2021.5, integrated with PLUMED[40].

535 To model the unresolved intracellular domain (residues 258–302), RoseTTAFold
536 on the Robetta server (https://robetta.bakerlab.org/) was employed for structure
537 prediction[41]. Based on secondary structure and transmembrane region predictions
538 from the protein sequence[42], TML6 (residues 220-236) was predicted to be a
539 transmembrane helix, as opposed to the loop observed in the cryo-EM map
540 (Supplementary Fig. 3). As such, two models were used to represent the mBOCT1
541 protein (residues 98-475). In the first model (model A), the intracellular domain
542 structure was taken from the Robetta model and added to the refined cryo-EM
543 structure. In the second model (model B), TML6 was presented as a helix, and both
544 the TML6 helix and the intracellular domain were combined with other
545 transmembrane helices from the refined cryo-EM structure. MODELLER was used to
546 combine the Robetta predictions with the refined cryo-EM structure[43]. For each model,

547 5000 models were generated and refined, while the one with the best DOPE score was
548 selected for further optimization using Maestro's protein preparation wizard
549 (Schrödinger, NY). The optimized model A and B were used for subsequent
550 simulations.
551
552 **All-atom molecular dynamics (MD) simulations**
553 All-atom MD simulations were performed on the refined cryo-EM structure of
554 mBOCT1, incorporating the intracellular domain predicted by the Robetta model.
555 These simulations were carried out in explicit solvents and lipid bilayers composed of
556 70% POPC and 30% cholesterol by molar ratio[44]. The protein was first aligned within
557 the membrane using the PPM 2.0 Web server before system assembly in
558 CHARMM-GUI[38,45-47]. The system was solvated in water, with Na^+ and Cl^- ions
559 added to neutralize the charge and maintain a physiological NaCl concentration of
560 150 mM. For the iron-bound (holo) system, one Fe^{2+} ion was added along with
561 balancing Cl^- ions.
562 The CHARMM36 force field was used to describe the protein, lipids, and ions,
563 while water was modeled using the CHARMM TIP3P water model[48,49]. Simulations
564 were conducted both with and without Fe^{2+} bound to the protein, and all simulation
565 systems are detailed in Supplementary Tables 1 and 3. After equilibration following
566 the CHARMM-GUI Membrane Builder protocol at 310.15 K[46,47], 3 replicas of 1 μs
567 and 15 replicas of 200 ns production runs were performed for apo systems, while 5
568 replicas of 500 ns runs were conducted for holo systems to assess ion binding. All

569 productive runs were performed in the NPT ensemble, maintaining a temperature of
570 310.15 K via Nosé-Hoover thermostat and a pressure of 1 bar using
571 Parrinello-Rahman coupling. Lennard-Jones interactions were truncated between 10
572 Å and 12 Å with a force-based switching method[50], and long-range electrostatics were
573 computed using the particle-mesh Ewald method with a grid size of 0.16 Å and
574 fourth-order interpolation[51]. Periodic boundary conditions were applied in all three
575 directions. The equations of motion were integrated using the leapfrog algorithm with
576 a 2 fs time step, saving trajectory data every 10 ps.
577
578 **Coarse-grained molecular dynamics (MD) simulations**
579 Coarse-grained MD simulations were performed using Martini Maker in
580 CHARMM-GUI, employing the same protein alignment and lipid composition as in
581 the all-atom simulations[38,39,52,53]. Systems were solvated in water, with 150 mM NaCl
582 added. The Martini3 force field was applied to describe the protein, lipids, water, and
583 ions[54]. Coarse-grained MD simulation systems and system compositions are provided
584 in Supplementary Table 1 and Supplementary Table 3, respectively.
585 Minimization and equilibration were carried out with gradually decreasing
586 position restraints on the protein and lipid heads, employing the Berendsen barostat,
587 v-rescale thermostat, and reaction-field electrostatics. Productive simulations of 100
588 μs were performed at 310.15 K in the NPT ensemble with a 20 fs time step, using
589 Parrinello-Rahman pressure coupling. To preserve the protein secondary structure, an
590 elastic network with a bond force constant of 500 kJ/(mol·nm^2) was applied to the

591 transmembrane helix backbones, with bond cutoffs set between 0.5 nm and 0.9 nm.

592

593 **Parallel cascade selection molecular dynamics (PaCS-MD)**

594 PaCS-MD simulations were employed to study ion transport in mBOCT1[55].
595 Supplementary Table 2 lists all PaCS-MD systems used in this study. The initial
596 conformations were selected from all-atom MD simulations, e.g. a frame with Fe^{2+}
597 bound at the binding site. Starting from each selected conformation, multiple short
598 MD simulations were performed for each system. MD frames were ranked based on
599 the depth of Fe^{2+} in the lipid bilayer, measured by the distance between the ion and
600 the center of mass of phosphate atoms in the extracellular lipid leaflet. The top-ranked
601 frame was used as the starting point for subsequent simulation rounds. Each round
602 consisted of 100 parallel MD simulations of 10 ns each, following the same settings
603 as the all-atom simulations. This iterative process continued until Fe^{2+} was released to
604 the intracellular side.

605

606 **Root mean square fluctuation (RMSF) and helicity analysis**

607 The RMSF of the protein backbone was calculated using the gmx rmsf command in
608 GROMACS to assess structural stability in the apo systems during all-atom MD
609 simulations. Helicity of transmembrane residues was evaluated using the gmx helix
610 command, with averages computed over the simulation duration.

611

612 **Root-mean-square deviation (RMSD)-based hierarchical clustering**

613 Hierarchical clustering was used to identify representative structural conformations
614 from both all-atom and coarse-grained MD simulations of apo systems. For all-atom
615 simulations, trajectories were concatenated, and frames were extracted every 500 ps.
616 For coarse-grained simulations, frames were extracted from 100 μs of trajectories at
617 20 ns intervals. All frames were superimposed using the backbone atoms/beads of
618 TM3 (residues 127–145) and TM9 (residues 364–384). The pairwise RMSD matrix
619 was computed for residues 220–302, encompassing TML6 and the intracellular
620 domain.

621 Clustering was performed using SciPy's hierarchical clustering algorithm,
622 applying an RMSD cutoff of 10 Å for all-atom simulations and 20 Å for
623 coarse-grained simulations[56]. The centroid frame of each cluster was selected, and
624 coarse-grained models were converted back to all-atom models using
625 CHARMM-GUI[38].

626

627 **Hydrogen bond analysis**

628 Hydrogen bonding dynamics were analyzed from concatenated PaCS-MD trajectories
629 exported every 100 ps. Water molecules in the hydration shell of the Fe^{2+} ion were
630 identified, and hydrogen bonds between the hydration shell and protein residues
631 (D169 and E193) were calculated using the HBond plugin in VMD[57]. The criteria for
632 hydrogen bonding were a donor-acceptor distance cutoff of 3.5 Å and a
633 donor-H-acceptor angle cutoff of 150°.

634

635 **Supplementary Information**

636 Supplementary Table 1. Non-biased molecular dynamics simulation systems.

637 Supplementary Table 2. All-atom parallel cascade selection molecular dynamics

638 (PaCS-MD) simulation systems.

639 Supplementary Table 3. Molecular dynamics simulation system compositions.

640 Supplementary Table 4. Protein backbone root mean squared deviations (RMSD)

641 from all-atom MD simulations.

642 Supplementary Table 5. Fe^{2+} ion RMSD from holo all-atom MD simulations.

643 Supplementary Table 6. mBOCT1–Fe^{2+} contact frequencies from MD simulations.

644 Supplementary Table 7. Penetration depth of Fe^{2+} ion in mBOCT1 from PaCS-MD.

645

646 Supplementary Figure 1. Sequence alignment between representative members of the

647 SLC22 family.

648 Supplementary Figure 2. Sequence alignment of BOCT1 across various species.

649 Supplementary Figure 3. Secondary structure and transmembrane topology prediction

650 from mBOCT1 sequence.

651 Supplementary Figure 4. Key amino acids that are vital for iron transport in

652 mBOCT1.

653 Supplementary Figure 5. Different conformations of TML6 in MD simulations: the

654 left panel shows the sideview, and the right panel shows the topview.

655 Supplementary Figure 6. Structural alignment of occluded mBOCT1 (cryo-EM, this

656 study), outward-open mBOCT1 (MD simulations), and inward-open mBOCT1 (MD

simulations).

Supplementary text: secondary structure and transmembrane topology prediction, simulation of apo mBOCT1, simulation of holo mBOCT1, parallel cascade selection molecular dynamics (PaCS-MD), homology modelling using hOCT1 as template.

Supplementary Movie 1: Fe^{2+} ion moving from the extracellular membrane lipid into the protein in model A, attracted by D336. The Fe^{2+} ion moves from D336 towards H200 in the last few seconds of the movie. D336 and H200 are labeled along the transport pathway.

In the movie, phosphate atoms in membrane lipids are represented as gray spheres, marking the membrane interface. Proteins are depicted as cyan cartoons, and Fe^{2+} ions are shown as red spheres.

Data availability

The cryo-EM map has been deposited in the Electron Microscopy Data Bank (EMDB) under accession number EMD-60664, and the coordinates have been deposited in the Protein Data Bank (PDB) under accession number 9IL4. Source data are provided with this paper.

References

678 32 Punjani, A., Rubinstein, J. L., Fleet, D. J. & Brubaker, M. A. cryoSPARC:
679 algorithms for rapid unsupervised cryo-EM structure determination. *Nat Methods* **14**,
680 290-296 (2017).
681 33 Adams, P. D. *et al.* PHENIX: a comprehensive Python-based system for
682 macromolecular structure solution. *Acta Crystallogr D Biol Crystallogr* **66**, 213-221
683 (2010).
684 34 Emsley, P. & Cowtan, K. Coot: model-building tools for molecular graphics.
685 *Acta Crystallogr D Biol Crystallogr* **60**, 2126-2132 (2004).
686 35 Pettersen, E. F. *et al.* UCSF ChimeraX: Structure visualization for researchers,
687 educators, and developers. *Protein Sci* **30**, 70-82 (2021).
688 36 Hoff, S. E., Thomasen, F. E., Lindorff-Larsen, K. & Bonomi, M. Accurate model
689 and ensemble refinement using cryo-electron microscopy maps and Bayesian
690 inference. *PLoS Comput Biol* **20**, e1012180 (2024).
691 37 Tribello, G. A., Bonomi, M., Branduardi, D., Camilloni, C. & Bussi, G.
692 PLUMED 2: New feathers for an old bird. *Computer Physics Communications* **185**,
693 604-613 (2014).
694 38 Jo, S., Kim, T., Iyer, V. G. & Im, W. CHARMM-GUI: a web-based graphical
695 user interface for CHARMM. *J Comput Chem* **29**, 1859-1865 (2008).
696 39 Lee, J. *et al.* CHARMM-GUI Input Generator for NAMD, GROMACS, AMBER,
697 OpenMM, and CHARMM/OpenMM Simulations Using the CHARMM36 Additive
698 Force Field. *J Chem Theory Comput* **12**, 405-413 (2016).

699 40 Abraham, M. J. *et al.* GROMACS: High performance molecular simulations
700 through multi-level parallelism from laptops to supercomputers. *SoftwareX* **1-2**, 19-25
701 (2015).
702 41 Baek, M. *et al.* Accurate prediction of protein structures and interactions using a
703 three-track neural network. *Science* **373**, 871-876 (2021).
704 42 Wang, S., Peng, J., Ma, J. & Xu, J. Protein Secondary Structure Prediction Using
705 Deep Convolutional Neural Fields. *Sci Rep* **6**, 18962 (2016).
706 43 Sali, A. & Blundell, T. L. Comparative protein modelling by satisfaction of
707 spatial restraints. *J Mol Biol* **234**, 779-815 (1993).
708 44 Ingólfsson, H. I. *et al.* Lipid organization of the plasma membrane. *J Am Chem*
709 *Soc* **136**, 14554-14559 (2014).
710 45 Lomize, M. A., Pogozheva, I. D., Joo, H., Mosberg, H. I. & Lomize, A. L. OPM
711 database and PPM web server: resources for positioning of proteins in membranes.
712 *Nucleic Acids Res* **40**, D370-376 (2012).
713 46 Wu, E. L. *et al.* CHARMM-GUI Membrane Builder toward realistic biological
714 membrane simulations. *J Comput Chem* **35**, 1997-2004 (2014).
715 47 Lee, J. *et al.* CHARMM-GUI Membrane Builder for Complex Biological
716 Membrane Simulations with Glycolipids and Lipoglycans. *J Chem Theory Comput* **15**,
717 775-786 (2019).
718 48 Best, R. B. *et al.* Optimization of the additive CHARMM all-atom protein force
719 field targeting improved sampling of the backbone φ, ψ and side-chain χ(1) and χ(2)
720 dihedral angles. *J Chem Theory Comput* **8**, 3257-3273 (2012).

721 49 Jorgensen, W. L., Chandrasekhar, J., Madura, J. D., Impey, R. W. & Klein, M. L.
722 Comparison of simple potential functions for simulating liquid water. *The Journal of*
723 *Chemical Physics* **79**, 926-935 (1983).
724 50 Steinbach, P. J. & Brooks, B. R. New spherical-cutoff methods for long-range
725 forces in macromolecular simulation. *Journal of Computational Chemistry* **15**,
726 667-683 (1994).
727 51 Essmann, U. *et al.* A smooth particle mesh Ewald method. *The Journal of*
728 *Chemical Physics* **103**, 8577-8593 (1995).
729 52 Qi, Y. *et al.* CHARMM-GUI Martini Maker for Coarse-Grained Simulations with
730 the Martini Force Field. *J Chem Theory Comput* **11**, 4486-4494 (2015).
731 53 Hsu, P. C. *et al.* CHARMM-GUI Martini Maker for modeling and simulation of
732 complex bacterial membranes with lipopolysaccharides. *J Comput Chem* **38**,
733 2354-2363 (2017).
734 54 Souza, P. C. T. *et al.* Martini 3: a general purpose force field for coarse-grained
735 molecular dynamics. *Nat Methods* **18**, 382-388 (2021).
736 55 Harada, R. & Kitao, A. Parallel Cascade Selection Molecular Dynamics
737 (PaCS-MD) to generate conformational transition pathway. *J Chem Phys* **139**, 035103
738 (2013).
739 56 Virtanen, P. *et al.* SciPy 1.0: fundamental algorithms for scientific computing in
740 Python. *Nat Methods* **17**, 261-272 (2020).
741 57 Humphrey, W., Dalke, A. & Schulten, K. VMD: visual molecular dynamics. *J*
742 *Mol Graph* **14**, 33-38, 27-38 (1996).

Acknowledgments

We are grateful to Jiawei Wang from the School of Life Sciences, Bailong Xiao from the School of Pharmaceutical Sciences at Tsinghua University, and Daohua Jiang from the University of Chinese Academy of Science for their helpful discussions and sharing of reagents. We also acknowledge Shuimu BioSciences for their cooperation in cryo-EM data collection. This work has been supported by the National Natural Science Foundation of China (Grants 32130048, 92157301 to L.C.), the Ministry of Science and Technology of China National Key R&D Programs (Grant 2022YFA0806503 and 2024YFA1306103 to L.C.), a private donation from the Tsinghua University Education Foundation (Grant 202011 to L.C.), a Collaborative Fund from CytoCraft Biotech Co. and the Tsinghua-Foshan Innovation Special Fund (Grant 20229990133 to L.C.), as well as the Tsinghua Precision Medicine Foundation (Grant No.2022TS013). W.W. was partially supported by the SGUnited Jobs Initiative (Grant P20J3d1006) from the National Research Foundation Singapore. Both W.W. and H.F. were supported by the Biomedical Research Council of A*STAR, Singapore. The computational work for this article was performed using the resources of the National Supercomputing Centre, Singapore (https://www.nscc.sg).

Author contributions

L.C. conceived the project. J.C., L.C., X.L., and H.F. designed the experiments. J.C.

765 performed the purification experiments. J.C. and S.Z. prepared the cryo-EM samples.
766 J.C. collected the cryo-EM data. S.Z. and J.C. calculated the EM map. J.C., X.L., and
767 S.Z. built the model. J.C. carried out the functional assays *in vitro* and *in vivo*. W.W.
768 and H.F. conducted the MD simulations. J.C., S.Z., W.W., L.T., L.T., K.G., B.L.,
769 A.E., H.F., X.L., and L.C. analyzed and discussed the data. L.C., J.C., X.L., and H.F.
770 wrote the manuscript.
771
772 **Competing interests**
773 The authors declare no competing interests.
774
775 **Correspondence and requests for materials** should be addressed to Ligong Chen.
776
777
778
779
780
781
782
783
784

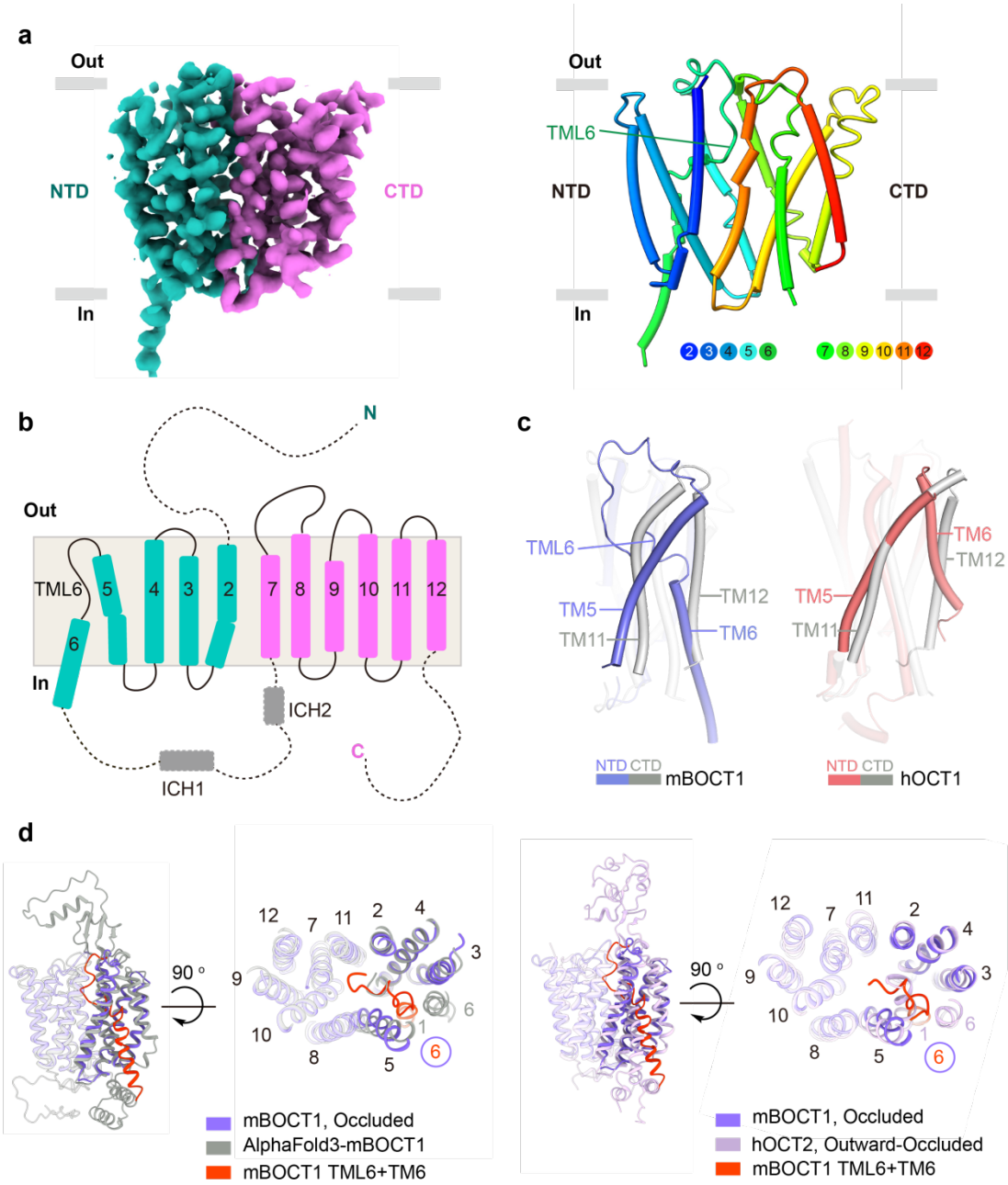

Fig. 1 | Overall structure of mBOCT1.

a, Cryo-EM map and model of mBOCT1 monomer. Left: Cryo-EM map showing the NTD (green), CTD (magenta), and membrane environment (gray rectangles). Right: Model of mBOCT1 in rainbow colors, with each color corresponding to a TM (indicated by circles of matching color). TML6 is shown as a straight line. **b,** Topology of mBOCT1 monomer, with NTD (green) and CTD (magenta). The dashed

line indicates unresolved regions. **c,** Structure alignments of NTD and CTD in mBOCT1 (this study) and hOCT1 (PDB: 8jtz). Non-transparent TMs (TM5, TM6, TML6, TM11, and TM12) are indicated by straight lines, while other regions are 80% transparent. mBOCT1 lacks pseudo-symmetric properties in its NTD and CTD. **d,** Structural alignment of mBOCT1 cryo-EM structure (purple) with AlphaFold3-predicted mBOCT1 (gray) and hOCT2 cryo-EM structure (PDB: 8et9) (purple). TML6 and TM6 in mBOCT1 are shown in red. Aligned TMs are labeled in black; unaligned segments are labeled in colors corresponding to their structures.

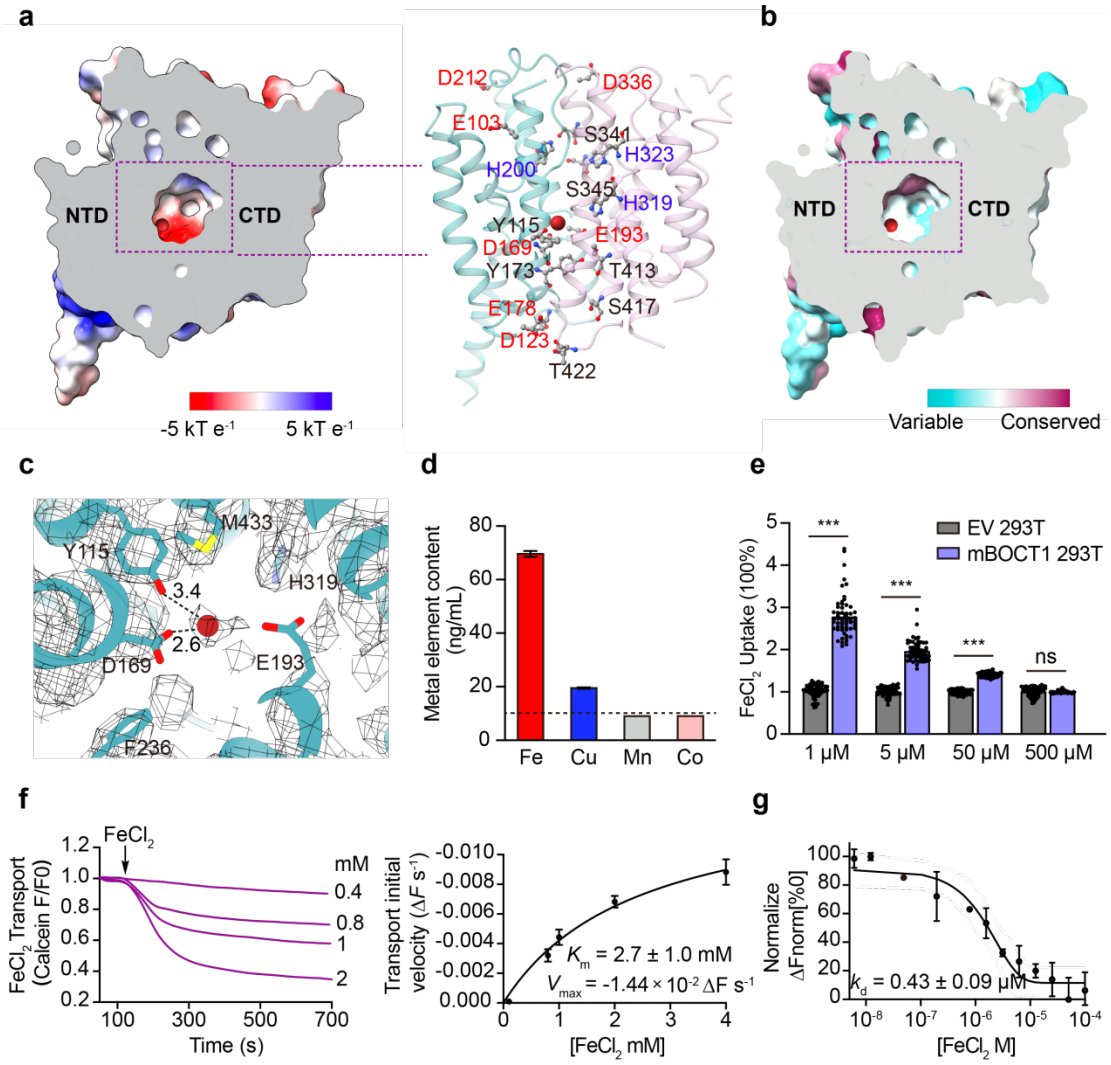

Fig. 2 | Structural analysis and substrate identification of mBOCT1.

a, Sliced view of the binding pocket showing surface electrostatic potential and polar residues. Fe^{2+} ion is shown as a red sphere; amino acids are depicted as sticks. The color bar indicates electrostatic potential. **b,** Sliced view showing variability of mBOCT1 compared to selected SLC22 family members, calculated by Consurf. The Fe^{2+} ion is shown as a red sphere; the color bar represents conservation levels. **c,** Extra density and surrounding residues in the mBOCT1 transport pathway. **d,** Metal ion content in mBOCT1 (cryo-EM sample preparation), detected by ICP-MS. Metal

809 content below 10 ng/mL (dashed line) is considered unreliable. Data are presented as
810 mean ± SD (n = 3). **e,** Cellular $FeCl_2$ uptake assay in mBOCT1-expressing HEK293T
811 cells, normalized to EV controls. Data are shown as mean ± SEM (n>3). Unpaired
812 *t*-test: $*p < 0.05$, $**p < 0.01$, $***p < 0.001$. **f,** Fe^{2+} transport by mBOCT1 in
813 calcein-containing liposomes. Time-course curves are averaged from n=3 independent
814 experiments. Initial velocity was obtained from the linear phase of the time-course
815 curve and fitted using the Michaelis-Menten formula in GraphPad Prism. Data are
816 Mean ± SD. **g,** $FeCl_2$ binding affinity of mBOCT1, detected by MST. Data are mean
817 ± SD (n = 3).
818
819
820
821
822
823
824
825
826
827

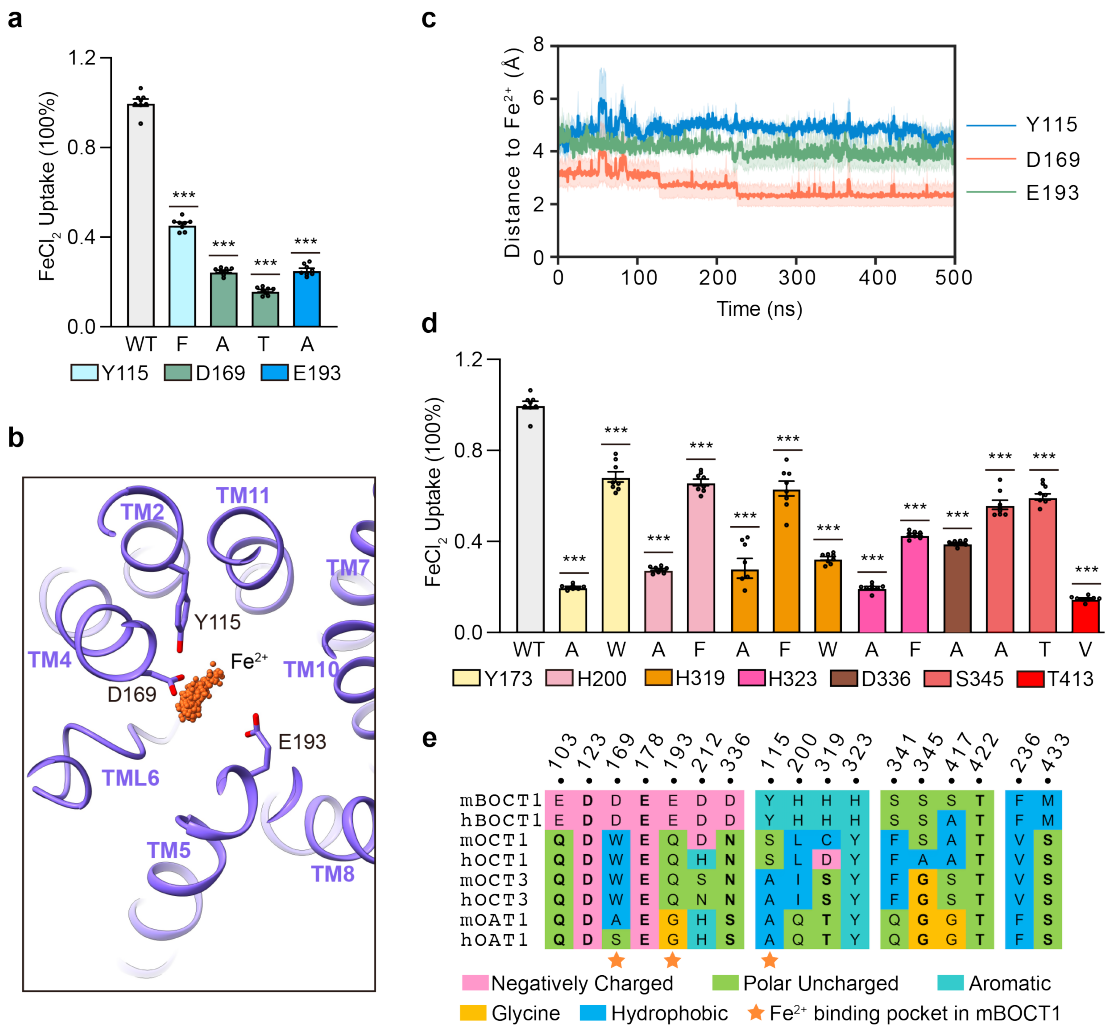

Fig. 3 | Substrate binding verification in mBOCT1 through mutations and MD simulations.

a, Fe^{2+} transport activity of binding pocket mutations. Data are mean ± SEM (n>3). Unpaired *t*-test: $*p < 0.05$, $**p < 0.01$, $***p < 0.001$. **b,** Fe^{2+} in the mBOCT1 binding pocket from all-atom MD simulations. **c,** Distances between Fe^{2+} and binding site residues (Y115, D169, E193) during 5 replicas of 500 ns holo MD simulations. Solid lines show the mean; shaded bands indicate SE across 5 replicas. **d,** Fe^{2+} transport activity of pathway mutations. Data are mean ± SEM (n>3). Unpaired *t*-test: $*p < 0.05$, $**p < 0.01$, $***p < 0.001$. **e,** Sequence alignment of key Fe^{2+}-transport residues

837 between mBOCT1 and selected SLC22 members. Residues are color-coded by

838 properties.

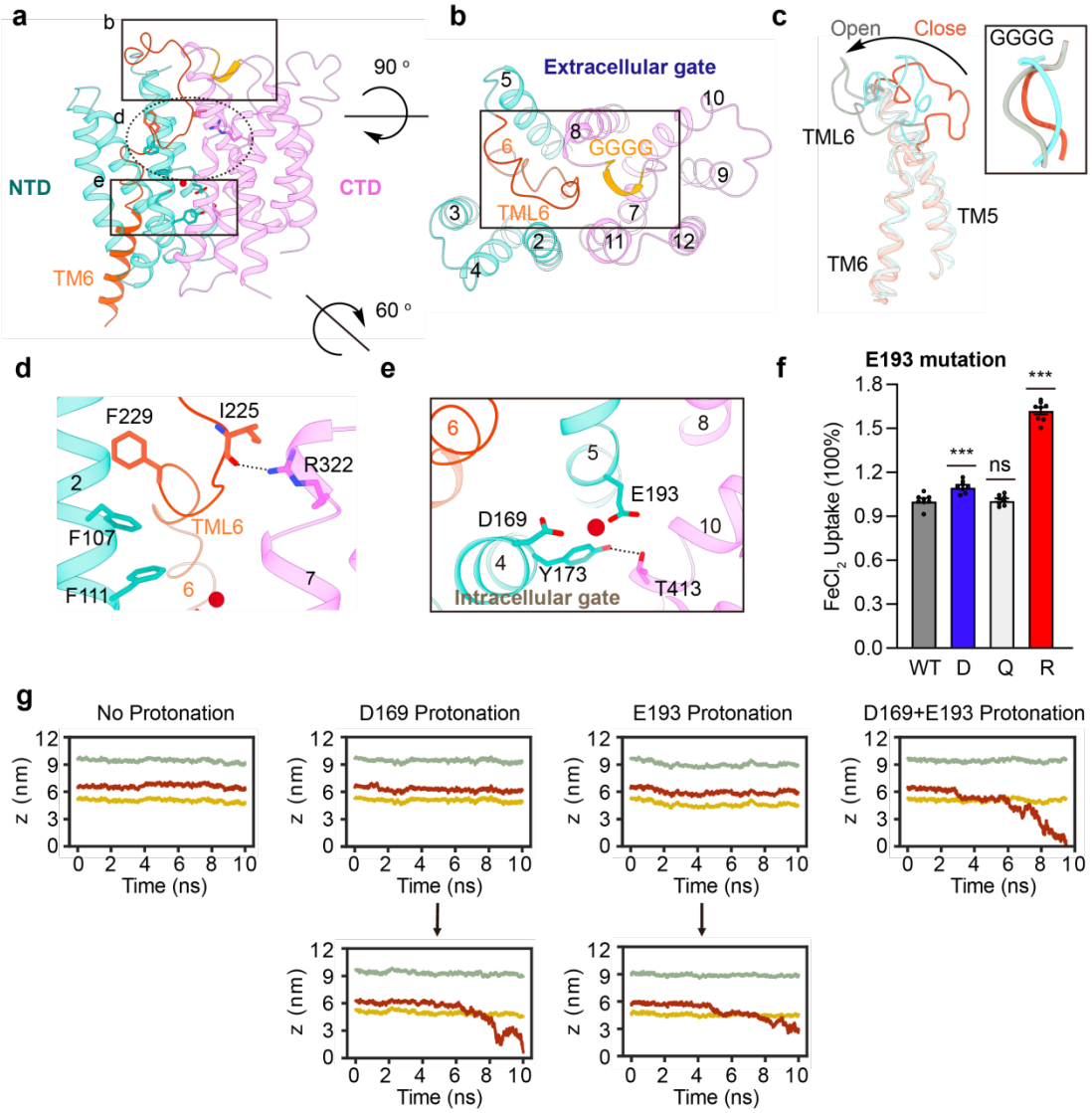

Fig. 4 | Substrate transport mechanism of mBOCT1.

a, Side view of the overall mBOCT1 structure. **b,** Top view of mBOCT1; the black box highlights the b region shown in panel a. TML6 and the GGGG motif form the extracellular transport gate. **c,** Structural diversity of TML6 in coarse-grained MD simulations. TML6 in the open state (gray) permits Fe^{2+} entry; in the closed state (red), it blocks transport. **d,** Zoomed view of region d (panel a) showing TML6 interactions with other TMs. Hydrogen bond: I225 (TML6) with R322 (TM7). Hydrophobic interactions: F229 (TML6) with F107 and F111 (TM2). **e,** Zoomed view of region e

847 (panel a) showing the intracellular transport gate formed by Y173–T413 hydrogen
848 bonding. **f,** Fe^{2+} transport activity of E193 mutations. Data are mean ± SEM (n>3).
849 Unpaired *t*-test: **p* < 0.05, ***p* < 0.01, ****p* < 0.001. **g,** Protonation effects on Fe^{2+}
850 transport in mBOCT1 observed in parallel cascade selection molecular dynamics
851 (PaCS-MD) simulations. PaCS-MD was conducted to investigate the Fe^{2+} ion
852 transport in mBOCT1 through multiple rounds of short parallel simulations. For each
853 round, 100 short MD simulations of 10 ns each were conducted. All MD frames were
854 collected and ranked by the penetration depth of Fe^{2+} ions in the lipid bilayer. The
855 top-ranked frame was utilized as the starting frame for the next round of PaCS-MD
856 simulations. For each system (System 11.1-11.4 in Supplementary Table 2), the Fe^{2+}
857 trajectory from the simulation with the deepest ion penetration is presented in the plot.
858 Green: extracellular phospholipid layer; yellow: intracellular layer; red: Fe^{2+}
859 trajectory.
860

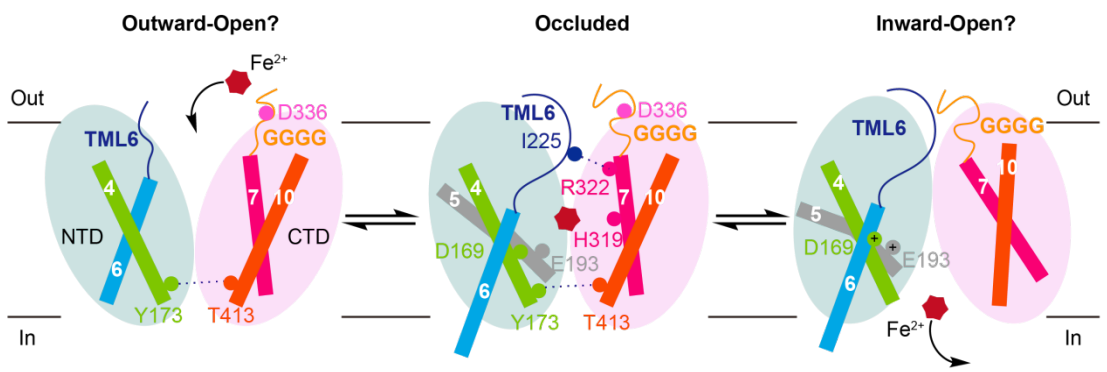

861 **Fig. 5 | Hypothetical mBOCT1 Fe^{2+} transport model.**

862 The outward-open and inward-open conformations of mBOCT1 are hypothetical, and
863 the occluded conformation is a simplified representation of the mBOCT1 cryo-EM
864 structure. The NTD and CTD of mBOCT1 are shown in light green and light red,
865 respectively. TMs are represented as rectangles in distinct colors, loops as lines,
866 amino acid residues as spheres, and Fe^{2+} as a hexagon. Plus signs indicate protonation,
867 while "out" and "in" denote the extracellular and intracellular environments,
868 respectively.

869

870 **Supplementary information**

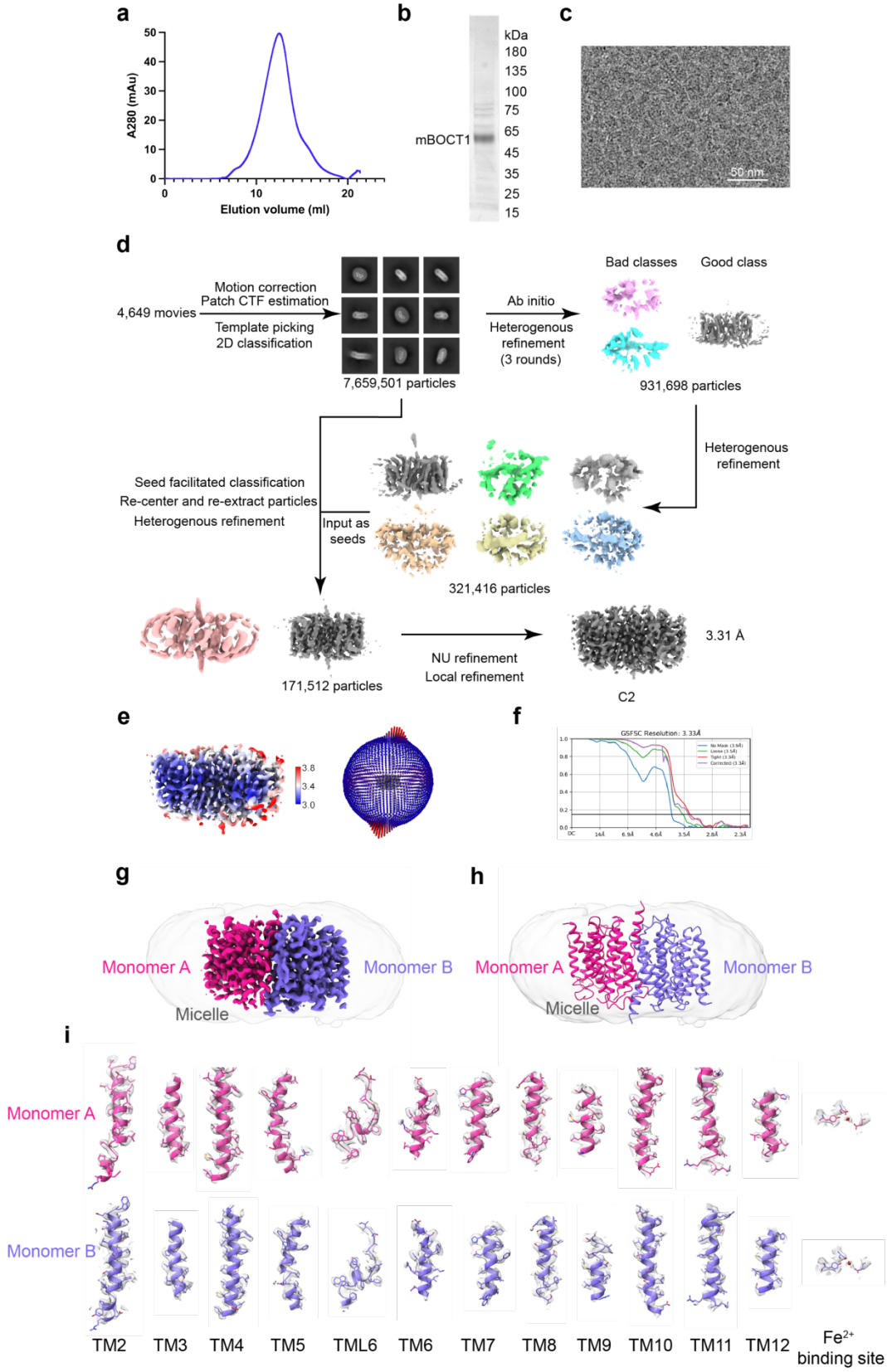

871

872 **Extended Data Fig. 1 | Cryo-EM structure determination of mBOCT1.**

873 **a,** Size exclusion chromatography (SEC) profile of mBOCT1. **b,** SDS-PAGE analysis
874 of peak fractions from the SEC of mBOCT1. **c,** Representative cryo-EM image of
875 mBOCT1 captured at 300 kV. **d,** Workflow for single-particle analysis of mBOCT1
876 using cryoSPARC. **e,** Local resolution estimation and angular distribution of
877 mBOCT1 in cryo-EM data. **f,** FSC curve of mBOCT1. **g,** Cryo-EM map of the
878 mBOCT1 dimer. **h,** Model of the mBOCT1 dimer. **i,** Density map of TMs and Fe^{2+}
879 binding site in mBOCT1, depicted as a gray surface.
880

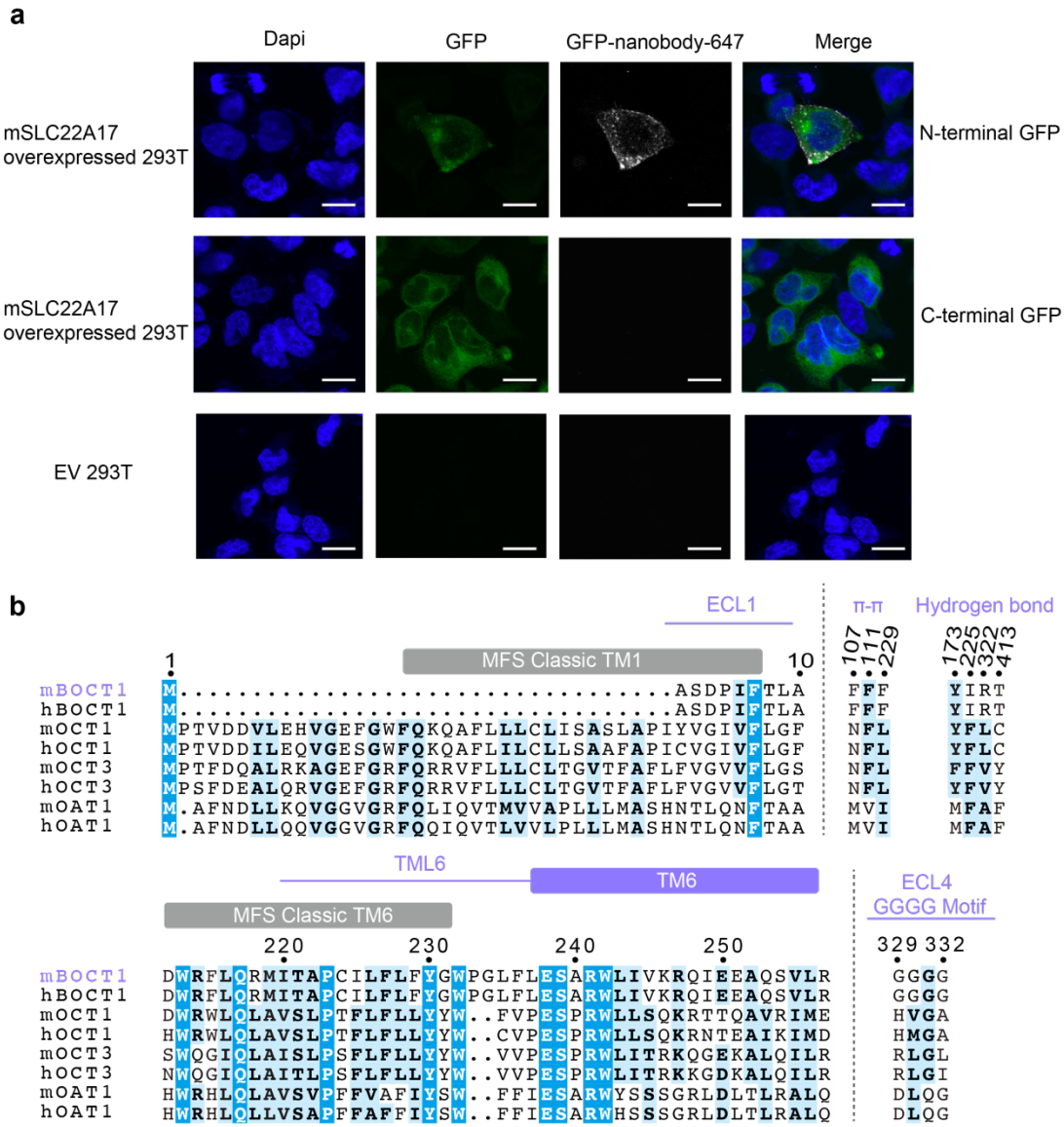

881 **Extended Data Fig. 2 | Structure verification *in vivo* and sequence alignment of**

882 **mBOCT1.**

883 **a,** Surface staining of mBOCT1 tagged with N-terminal or C-terminal GFP in stable

884 293T cell lines and EV 293T cell lines via immunofluorescence. DAPI indicates cell

885 nuclei, GFP represents mBOCT1-GFP, and GFP-nanobody-647 shows the GFP

886 nanobody labeled with Alexa Fluor 647. Scale bar: 10 μm. **b,** Sequence alignment of

887 unique regions in mBOCT1 compared to selected SLC22 family members. TMs are

888 represented as rectangles above the sequences, loops as lines. Secondary structural
889 features of mBOCT1 are shown in purple, while those of traditional MFS transporters
890 are in gray.
891

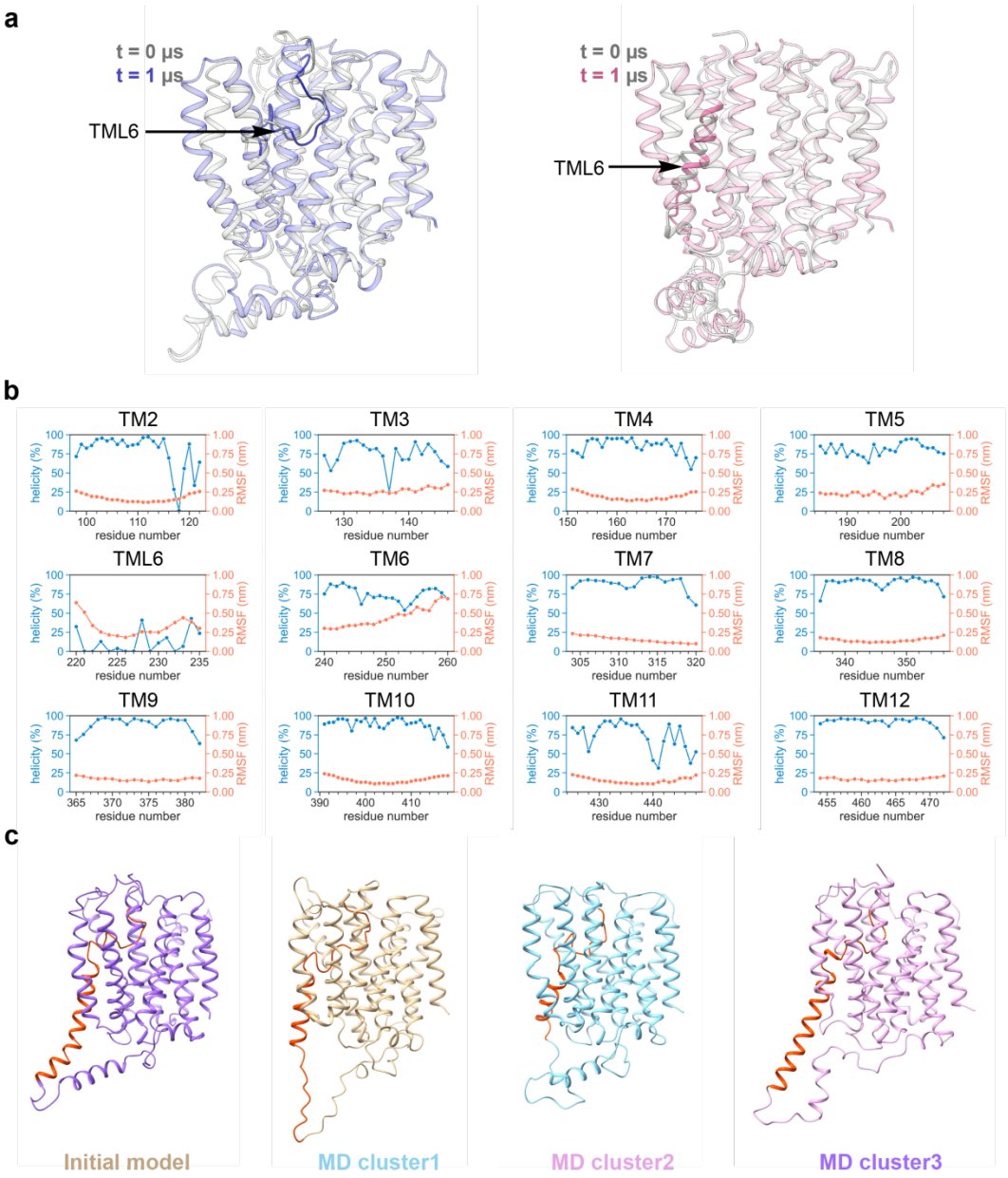

892

893 **Extended Data Fig. 3 | Structural stability of TML6 and TM6 in MD simulations.**

894 **a,** Stability of TML6 in loop or helix form observed in apo MD simulations (System 1

895 and 2 in Supplementary Table 1). The time scale is 1 μs. TML6 is marked by an

896 arrow, and other structural segments are set to 80% transparency. **b,** RMSF and

897 helicity of the 11 TMs in mBOCT1 from all-atom MD simulations. **c,** Various

898 conformational states of TML6 and TM6 in mBOCT1 observed in MD simulations.

899 TML6 and TM6 are highlighted in red.

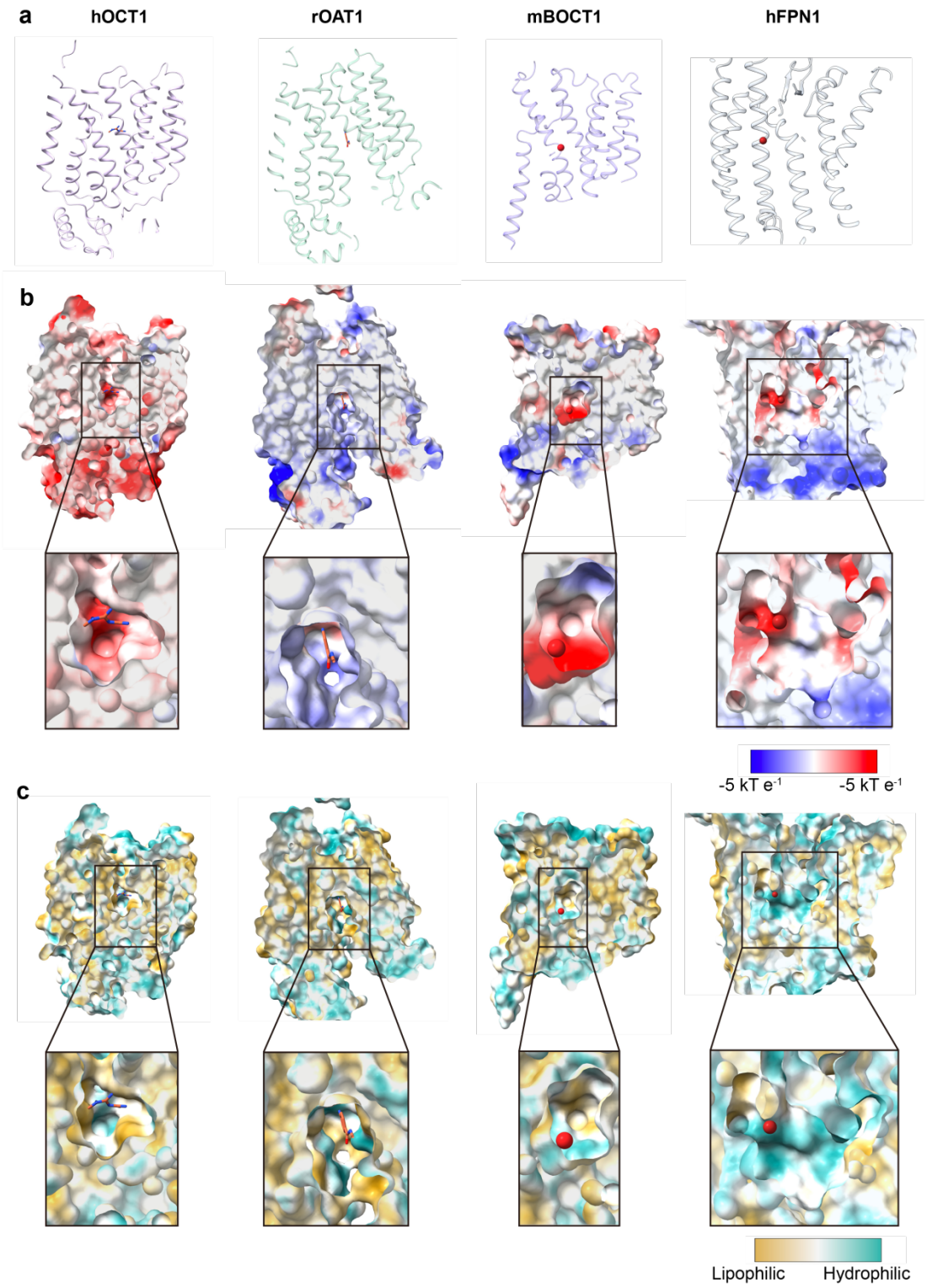

900 **Extended Data Fig. 4 | Structural comparison of mBOCT1 with selected SLC22**

901 **members and hFPN1.**

902 **a,** Models of hOCT1 (PDB: 8JTT), rOAT1 (PDB: 8SDY), mBOCT1 (this study), and

903 hFPN1 (PDB: 6WBV). **b,** Corresponding sliced views of surface potential and

904 magnified views of the binding pocket. A color key for electrostatic potential is
905 displayed below. **c,** Sliced views of hydrophilicity analysis and magnified views of
906 the binding pocket. A color key for hydrophobicity is displayed below.
907

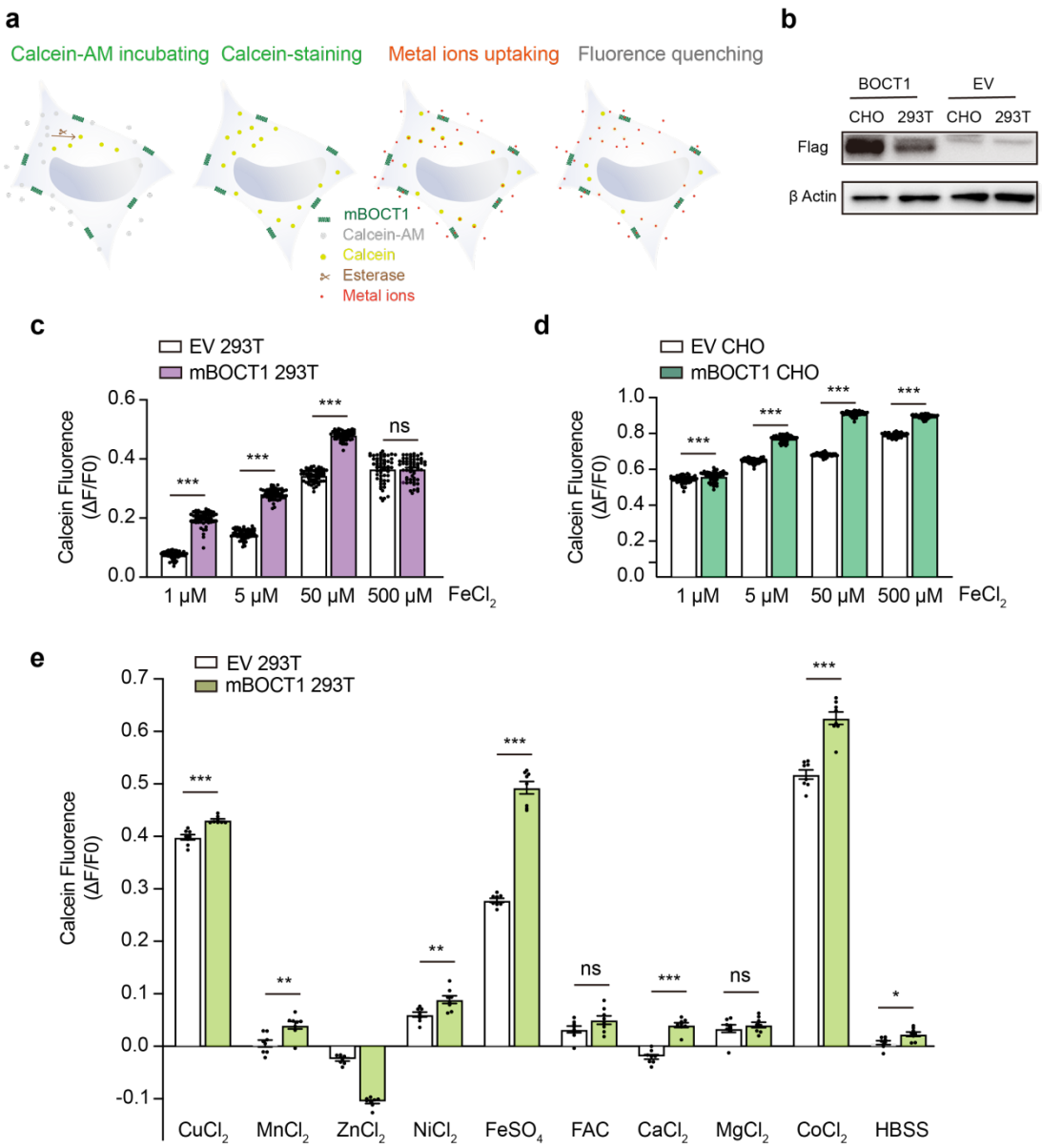

Extended Data Fig. 5 | Cellular uptake of mBOCT1 with metal ions compounds. **a,** Schematic of the cellular uptake assay using calcein. Non-fluorescent calcein-AM was incubated with mBOCT1 293T stable cell lines and converted into fluorescent calcein by esterases. Fluorescence quenching occurred upon metal ion transport into cells. **b,** Western blot validation of stable mBOCT1 overexpression in 293T and CHO cells. mBOCT1 was fused with an N-terminal Flag tag. **c,** Cellular uptake assay of mBOCT1-expressing HEK 293T stable cell lines with $FeCl_2$. Data are shown as Mean

915 ± SEM from n > 3 independent experiments. **d,** Cellular uptake assay of
916 mBOCT1-expressing CHO stable cell lines with $FeCl_2$. Data are shown as Mean ±
917 SEM from n > 3 independent experiments. **e,** Cellular uptake assay of HEK 293T
918 stable cell lines with various metal ion compounds. Data are shown as Mean ± SEM
919 from n > 3 independent experiments.
920 Significance for panels c–e was analyzed using an unpaired *t*-test. Significance levels:
921 $*p < 0.05$, $**p < 0.01$, and $***p < 0.001$.
922

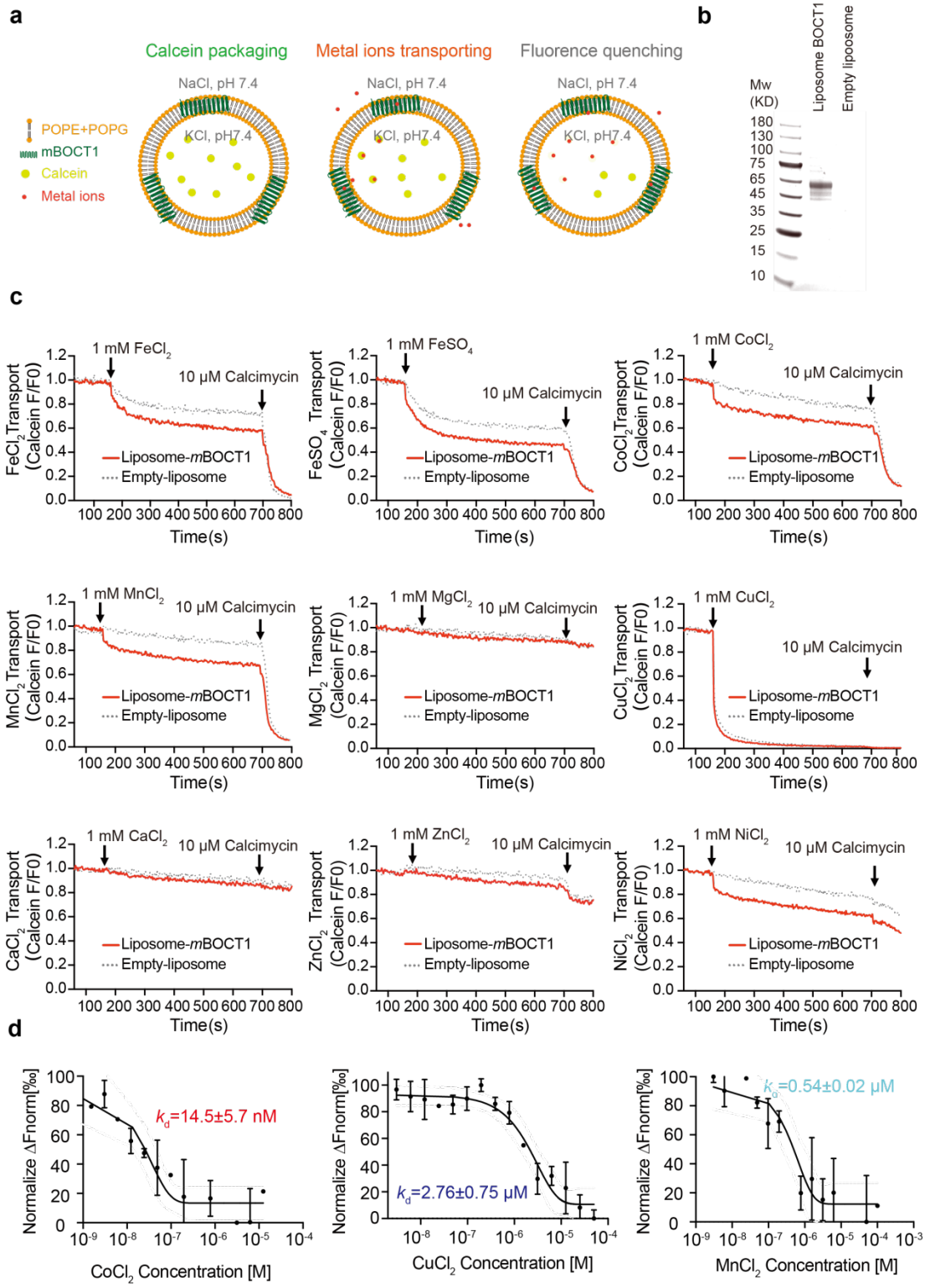

Extended Data Fig. 6 | Liposome transport and MST binding assay of mBOCT1 with metal ions compounds.

a, Schematic of the liposome transport assay using calcein fluorescence as an

927 indicator. Purified mBOCT1 was reconstituted into liposomes composed of POPE and
928 POPG, containing calcein. Fluorescence quenching occurs upon metal ion transport or
929 when the ionophore calcimycin is added. **b,** Verification of mBOCT1 reconstitution
930 by SDS-PAGE. **c,** Representative dynamic transport curves of various metal ions in
931 the mBOCT1 liposome system. Data were obtained from three independent replicates.
932 **d,** Binding curves for different metal ions with mBOCT1 measured by MST. Data
933 were obtained from three independent replicates.

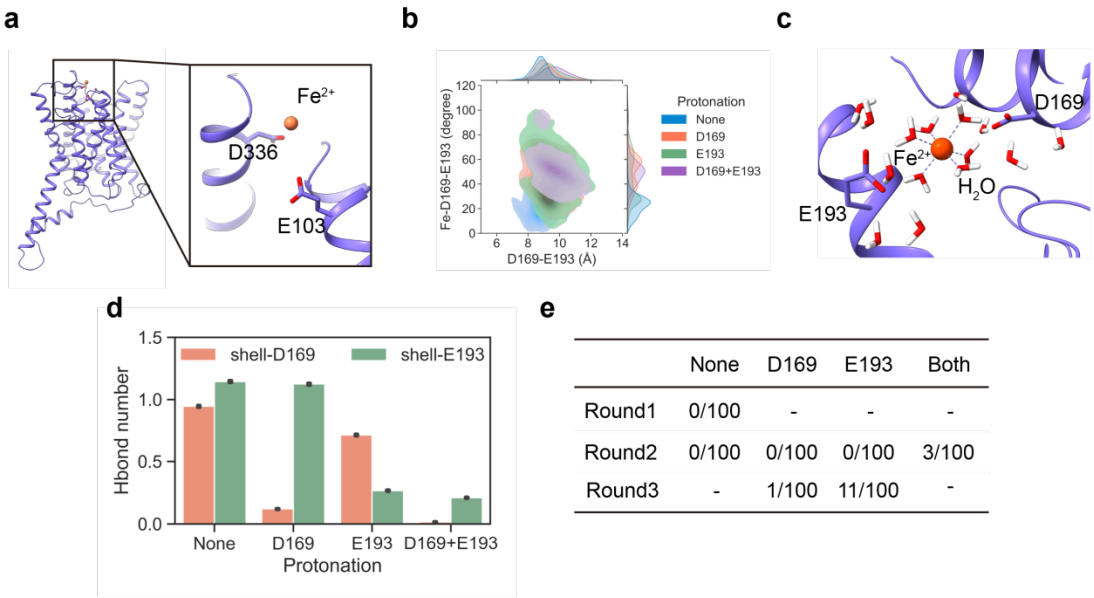

	None	D169	E193	Both
Round1	0/100	-	-	-
Round2	0/100	0/100	0/100	3/100
Round3	-	1/100	11/100	-

Extended Data Fig. 7 | Effect of D336 and the protonation of D169 and E193 on iron transport as indicated by MD simulations.

a, Residues at the entrance of the mBOCT1 transport pathway when Fe^{2+} enters the transporter in MD simulations. **b,** Distance and angle changes between D169-E193 and Fe^{2+}-D169-E193 upon protonation of D169 or E193. **c,** Surrounding water molecules around the Fe^{2+} binding site in the mBOCT1 transport pathway. **d,** Hydrogen bonds between the hydration shell and D169/E193 upon protonation of D169 or E193. **e,** Number of Fe^{2+} release events (out of 100 parallel runs) in three rounds of PaCS-MD simulations upon protonation of D169 or E193.

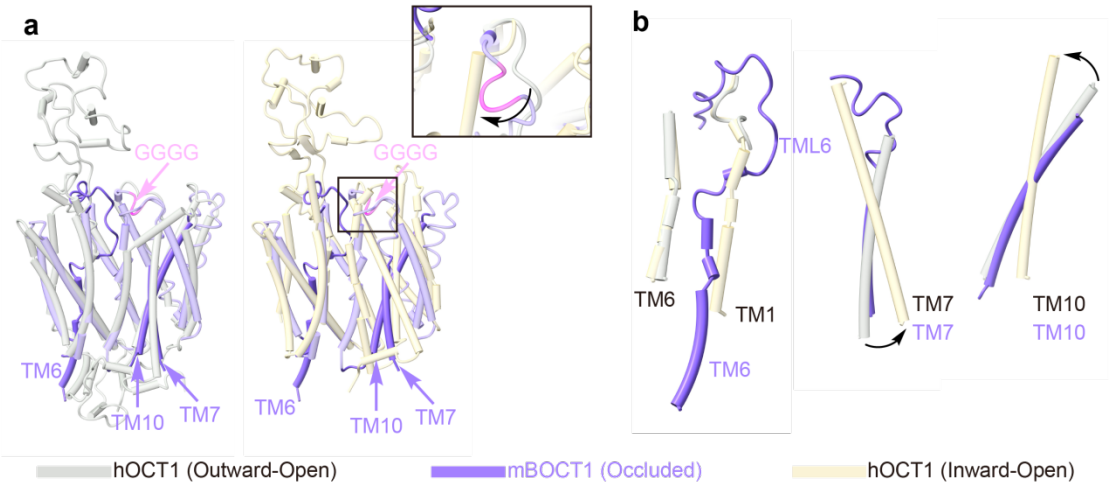

Extended Data Fig. 8 | Structure comparisons of mBOCT1 with hOCT1 in different conformations.

a, Structural alignments of mBOCT1 with outward-open hOCT1 (PDB: 8et6) and inward-open hOCT1 (PDB: 8sc1). Important helices and motifs essential for mBOCT1 transport are highlighted. **b,** Structural alignments of TML6, TM6, TM7, and TM10 of mBOCT1 with the corresponding TMs in outward-open and inward-open hOCT1.

951 **Table 1. Cryo-EM data collection, refinement, and validation statistics**

	***m*BOCT1**
Data collection and processing	
Microscope	Titan Krios G3i
Camera	K3
Spherical Aberration (mm)	0.01
Magnification	64000
Voltage (kV)	300
Electron exposure (e-/Å^2)	50
Exposure time (s)	2.53
Defocus range (μm)	-1.2 to -1.5
Pixel size (super resolution Å)	0.54
Slit width (eV)	20
Frame	32
Micrographs	4649
Autopicked particles	7659501
Particles in final refinement	178900
Symmetry imposed	C2
FSC threshold	0.143
Map sharpening B factor (Å^2)	-138.7
Map resolution (Å)	3.3（cryoSparc）
Map resolution range (Å)	
FSC 0.5, unmasked/masked	6.3-3.9
FSC 0.143, unmasked/masked	3.5-3.4
Refinement	
Initial model used (PDB code)	-
Model composition	
Non-hydrogen atoms	4946
Protein residues	666
Ligands	Fe:2
Water	N/A
B factors (Å^2)	
Protein	99.54
Ligand	93.71
Water	-
R.m.s. deviations	
Bond lengths (Å)	0.003
Bond angles (°)	0.622
Validation	
Rotamers outliers (%)	0
Molprobity score	2.05
CaBLAM Score	2.02
Clashscore	13.08
Ramachandran plot	
Favored (%)	93.62%
Allowed (%)	6.38%
Disallowed (%)	0

952